AD-A115 871 NORWEGIAN DEFENCE RESEARCH ESTABLISHMENT KJELLER F/G 20/4
AERODYNAMICS OF CONES AT HIGH ANGLES OF ATTACK IN LOW SUBSONIC --ETC(U)
JUN 81 J I BOTNAN
UNCLASSIFIED NDRE/PUB-81/1004 NL

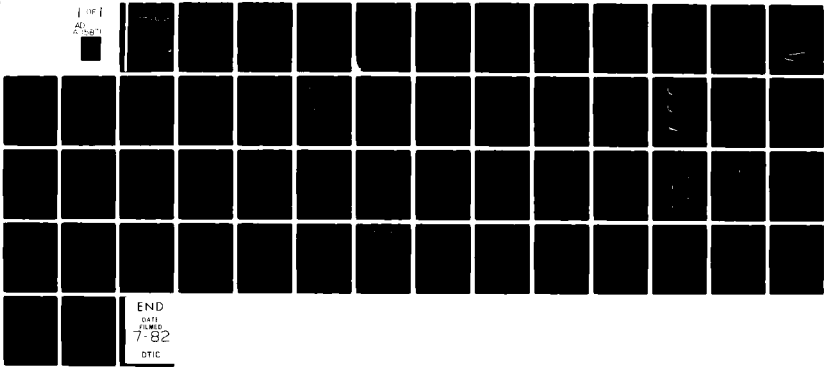

END
DATE FILMED
7-82
DTIC

AERODYNAMICS OF CONES AT HIGH ANGLES OF ATTACK IN LOW SUBSONIC FLOW

BY

JAN IVAR BOTNAN

NDRE/PUBS-81/1004

ISSN 0085-4301

FORSVARETS FORSKNINGSINSTITUTT
NORWEGIAN DEFENCE RESEARCH ESTABLISHMENT
P O Box 25 - N-2007 Kjeller, Norway

AERODYNAMICS OF CONES AT HIGH ANGLES OF ATTACK IN LOW SUBSONIC FLOW

by

Jan Ivar Botman

NDRE/PUBL–81/1004
ISSN 0085–4301

FORSVARETS FORSKNINGSINSTITUTT
NORWEGIAN DEFENCE RESEARCH ESTABLISHMENT
P O Box 25 - N-2007 Kjeller, Norway

JUNE 1981

NORWEGIAN DEFENCE RESEARCH ESTABLISHMENT (NDRE)
FORSVARETS FORSKNINGSINSTITUTT (FFI)
POST OFFICE BOX 25
N-2007 KJELLER, NORWAY

UNCLASSIFIED
SECURITY CLASSIFICATION OF THIS PAGE
(when data entered)

REPORT DOCUMENTATION PAGE

1) PUBL/REPORT NUMBER	2) SECURITY CLASSIFICATION	3) NUMBER OF PAGES
NDRE/PUBL-81/1004	UNCLASSIFIED	58
1a) JOB REFERENCE	2a) DECLASSIFICATION/DOWNGRADING SCHEDULE	
435-VM/131	-	

4) TITLE
AERODYNAMICS OF CONES AT HIGH ANGLES OF ATTACK IN LOW SUBSONIC FLOW

5) NAMES OF AUTHOR(S) IN FULL (surname first)
BOTNAN, Jan Ivar

6) DISTRIBUTION STATEMENT
Approved for public release. Distribution unlimited.
(Offentlig tilgjengelig)

7) INDEXING TERMS

IN ENGLISH:	IN NORWEGIAN
a) Three-dimensional boundary layer	a) Tredimensjonalt grensesjikt
b) High angle of attack	b) Store angrepsvinkler
c) Side forces	c) Sidekrefter
d) Subsonic	d) Subsonisk
e) Separated flow	e) Separert strøm

THESAURUS REFERENCE:

8) ABSTRACT (continue on reverse side if necessary)

This report is a theoretical study of various phenomena observed in the low subsonic regime when a slender cone of revolution is pitched to high angles of attack. Three-dimensional boundary layers are calculated up to the line of primary separation. The structure of the separated wake is obtained with a two-dimensional model and the results are used as input in a leeside boundary layer calculation. This calculation is carried on to the line of secondary separation. The positions of separation are compared with experimental results. The wake is found to be unstable at the angles of attack where strong asymmetric forces are observed. A stability analysis of the boundary layer rules out streamwise-directed vortices as a contributor to the asymmetric forces.

9) DATE	AUTHORIZED BY	POSITION
8 June 1981		Superintendent

UNCLASSIFIED
SECURITY CLASSIFICATION OF THIS PAGE
(when data entered)

CONTENTS

AERODYNAMICS OF CONES AT HIGH ANGLES OF ATTACK IN LOW SUBSONIC FLOW

SUMMARY

This report is a theoretical study of various phenomena observed in the low subsonic regime when a slender cone of revolution is pitched to high angles of attack. Three-dimensional boundary layers are calculated up to the line of primary separation. The structure of the separated wake is obtained with a two-dimensional model and the results are used as input in a leeside boundary layer calculation. This calculation is carried on to the line of secondary separation. The positions of separation are compared with experimental results. The wake is found to be unstable at the angles of attack where strong asymmetric forces are observed. A stability analysis of the boundary layer rules out streamwise-directed vortices as a contributor to the asymmetric forces.

1 INTRODUCTION

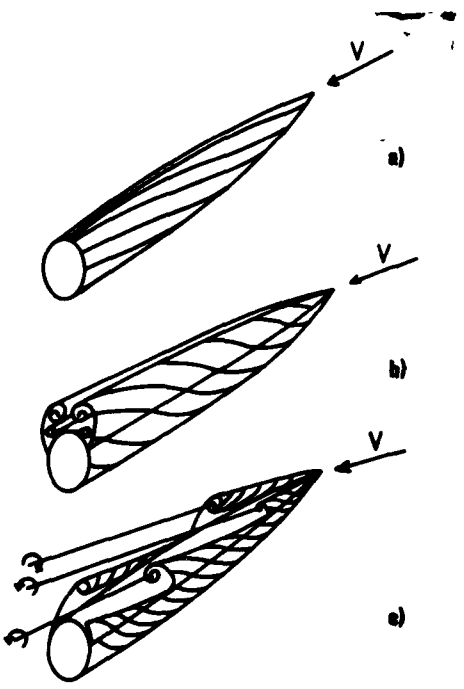

Figure 1.1 Vortex formation on the leeside of inclined body of revolution
a) attached, b) separated symmetric and c) steady asymmetric flow

Allan and Perkins (1) have classified flow around a slender body in four distinct groups depending on the angle of attack (Figure 1.1). At small angles the flow is attached. When the angle is increased, the boundary layer separates on the leeside, producing a symmetric vortex system. If the body is pitched to even higher angles, the symmetric structure breaks down. The vortex system is then steady, asymmetric and produces often undesired lateral forces even at zero sideslip. At very high angles of attack the wake becomes unsteady.

These phenomena are well known, but not well understood. The goal of the present thesis is to shed light on the flow patterns mentioned, with special attention to steady asymmetric flow. The unsteady phase will be just superficially treated.

Within the aircraft and missile industry, where the present requirements for manoeuvrability are difficult to meet, substantial research is carried out on slender bodies at high angles of attack. A number of experiments reveals connections between the asymmetric forces and important flow and geometry parameters. We shall now review the most important parameter effects.

1.1 Geometrical imperfections

Experiments with varying surface finish have been performed on a tangent ogive forebody (2). The surface roughness was found to have a large effect on vortex induced side-force.

When a body is tested in various roll-positions, the side-force may change direction for a range of roll angles (2,3,4,5). There is, as expected, no mirror symmetry in the results. Similar results are obtained when only a removable nose is rolled (5). This strongly indicates that nose-tip imperfections are the triggering mechanism for the asymmetric forces.

1.2 Mach number

From various experimental works (2,3,5), the following general trend can be outlined.

The side-force is most dominant in low subsonic flow. The effect is slightly reduced when the flow speed is increased and it drops drastically in the transonic domain. In the low supersonic region the force vanishes and does not reappear for higher speeds.

The side-force phenomenon is therefore primarily associated with subsonic speeds. The angle of attack for onset of asymmetric forces is rather insensitive to changes in Mach number.

1.3 Reynolds number

The Reynolds number may have a dominating influence on the side-force induced by asymmetric vortices. Keener *et al* (2) have performed experiments on a tangent ogive forebody at Reynolds number between $0.3 \cdot 10^6$ and $3.8 \cdot 10^6$ (based on base diameter). The Mach number was 0.25. The onset angle for significant side-forces was insensitive to the Reynolds number. This is consistent with other observations (3). The direction and magnitude, however, are strongly influenced by changes in Reynolds number. Coe *et al* (4), on the other hand, report a small Reynolds number sensitivity. Deffenbaugh and Koerner (6) find it difficult to determine the effect of the Reynolds number on maximum side-force.

There have also been performed experiments with boundary layer transition strips. Pick (7) finds a significant reduction in side-forces. This is inconsistent with the experiments of Keener *et al* (2) where side-forces indeed changed but were not generally reduced.

Jorgensen (3) used a grit ring to trip the boundary layer. The effect of this ring was small in the situations investigated. The lateral force as a function of the angle of attack changed when the grit ring was used, but the maximum force was nearly the same.

Increased Reynolds number and introduction of transition strips both promote earlier transition to turbulence. The various experiments, referred to here, give contradictory and confusing results. This is probably because the observed asymmetric forces are affected by the boundary layer in interaction with other flow characteristics. What is observed when increasing the Reynolds number or introducing transition strips is thus the result of a particular experimental situation rather than an expression of more basic properties.

The asymmetries occur in both laminar and turbulent flow, so the transition is presumably not an essential reason for the observed asymmetry. Local inflectional instability of the mean boundary layer profiles may be a contributer. This will be further investigated.

Adjusting the Reynolds number will probably not, in general, be a fruitful way to eliminate side-forces.

1.4 Nose-blunting

According to Keener *et al* (2) nose-blunting reduces the side-force on both tangent ogive and conical forebodies. Measurements on bodies with radius of curvature 6.35 mm and 12.7 mm, respectively, were performed. For a conical forebody the side-force reduction is quite independent of the nose radius. It is not so for the tangent ogive. The smaller radius of curvature is found to be the more effective in reducing side-forces. This is not in agreement with Wardlaw *et al* (8) who, after considering all experimental data up to 1975, conclude that blunt bodies show a lower level of asymmetric forces than sharp ones, but the degree of bluntness does not appear important.

As indicated previously, the side-force is probably due to the interaction of various effects. Some of these are not controlled in the experiments. We should therefore not be surprised by the somewhat peculiar results reported by Keener *et al* (2) for the blunted cone.

1.5 Theoretical contributions

There exist many semiempirical theories for separated flow around slender bodies of revolution. Angelucci's (9) multivortex model is one of the most successful. He uses experimental separation point locations as input in his incompressible and inviscid calculations. By using the cross-flow analogy (see Chapter 5) he converts a three-dimensional stationary problem to a two-dimensional unsteady one.

A method developed by Marshall and Deffenbaugh (10) is for the time being the most promising one. They, too, use the cross-flow analogy, but make boundary layer calculations instead of using empirical separation lines. Their model therefore incorporates viscous effects. The outer flow is modelled as a potential flow around an expanding circular cylinder superimposed on the flow of a number of point vortices describing the wake. The inner flow consists of an upstream and a downstream boundary layer. Where these separate, vorticity is fed into the inviscid wake. There is one empirical parameter used which reduces the wake vorticity compared with direct calculation.

The most apparent weakness of their model is its two-dimensionality. The three-dimensional separation process is more complex than separation in two dimensions (11). A two-dimensional approximation is therefore dubious. Marshall and Deffenbaugh (10) make a not too convincing separation line comparison with a finite difference solution.

We shall in the sequel try to improve the existing models by performing three-dimensional boundary layer calculations.

2 POTENTIAL FLOW

Prandtl's boundary layer approximation will be used in Chapter 4. As input there, a solution for the inviscid flow about the body is needed. This chapter is devoted to that problem.

If compressibility, in addition to viscosity, can be neglected, a substantial simplification of the equations results. We shall now establish the condition for this.

In adiabatic flow, the relation between changes in pressure (Δp) and density ($\Delta\rho$) is

$$\Delta p = \left(\frac{\partial p}{\partial \rho}\right)_s \Delta\rho \tag{2.1}$$

where s symbolizes entropy. According to Bernoulli's equation, Δp is of the order of ρv^2 in steady flow. The velocity of sound (c) in the fluid is $\sqrt{(\partial p/\partial\rho)_s}$. Equation (2.1) can then be rewritten to yield

$$\frac{\Delta\rho}{\rho} \sim \left(\frac{v}{c}\right)^2 \equiv M^2 \tag{2.2}$$

The fluid can be regarded as incompressible if $\Delta\rho/\rho \ll 1$, and this implies a small fluid velocity compared with that of the sound. For Mach 0.25 we have $\Delta\rho/\rho \sim 0.06$, and neglecting compressibility should be well justified below this speed. This must not be taken as a strict limit, however, because experience tells that compressibility effects are often negligible up to M = 0.5 (12).

In Chapter 1 we considered various observations made on slender bodies of revolution at high angle of attack. We shall, first of all, look for the origin of the often large asymmetric forces which are observed. These forces are most pronounced at speeds where compressibility is shown to be of little influence and diminish when the transonic region is entered. Thus it follows that compressibility cannot be the cause of the side-forces. It seems, on the contrary, that compressibility may reduce the effect. Our aim is to explain the side-force phenomenon and we shall make calculations under conditions where the asymmetries are observed to be substantial. Thus the assumption about incompressibility should not, under the given ambitions, be a limitation.

The inviscid flow can now be obtained by solving a perturbation problem where the flow velocity is given by $\vec{V} = \vec{V}_\infty - \nabla\varphi$. $\vec{V}_\infty$ is the free-stream velocity. The perturbation potential (φ) must satisfy Laplace equation (12)

$$\nabla^2\varphi = 0 \tag{2.3a}$$

with boundary conditions

$$\vec{V}\cdot\vec{n} = \vec{V}_\infty\cdot\vec{n} - \frac{\partial\varphi}{\partial n} = 0 \qquad \text{on the surface} \tag{2.3b}$$

and the regularity condition

$$|\text{grad}\varphi| \to 0 \qquad \text{at infinity.} \tag{2.3c}$$

$\vec{n}$ is the surface normal.

Analytical solutions are known just for a few special geometries. An almost classical method, developed by Hess and Smith (12) will now be outlined. The procedure is to convert the differential equation to an integral equation which is then solved numerically.

A well posed problem is obtained if we represent the solution by a single layer potential (13)

$$\varphi(\vec{x}) = \int_S \frac{\sigma(\vec{\xi})}{r}\, dS_\xi \tag{2.4}$$

$r = |\vec{x} - \vec{\xi}|$

where $\sigma(\vec{\xi})$ is the source strength over the surface S. It is readily seen that this potential satisfies the Laplace equation outside the body.

$$\nabla_x^2 \varphi(\vec{x}) = \int_S \sigma(\vec{\xi}) \nabla_x^2 (\frac{1}{r})\, dS_\xi = -4\pi \int_S \sigma(\vec{\xi})\, \delta(\vec{x} - \vec{\xi}) dS_\xi = 0, \text{ for } \vec{x} \notin S \tag{2.5}$$

The boundary condition is given as the normal derivative of the perturbation potential on the surface and from equation (2.4) we have

$$\frac{\partial \varphi}{\partial n}\Big|_S = -2\pi\sigma(\vec{x}) + \int_S \sigma(\vec{\xi}) \frac{\partial}{\partial n}(\frac{1}{r}) dS_\xi \tag{2.6}$$

The first term on the right-hand side arises from the limiting process of approaching the surface. When equation(2.6) is inserted, the boundary condition (2.3b) yields

$$2\pi\sigma(\vec{x}) - \int_S \frac{\partial}{\partial n}(\frac{1}{r}) \sigma(\vec{\xi}) dS_\xi = -\vec{n} \cdot \vec{V}_\infty \tag{2.7}$$

This is a Fredholm integral equation of second kind with the source density $\sigma(\vec{\xi})$ as the unknown function.

The equation is linear and we can split the problem into axisymmetric flow and cross flow. These can be handled separately and the total solution is obtained by superposition.

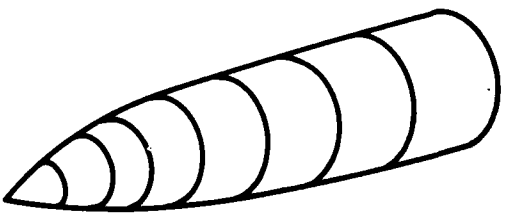

Figure 2.1 The surface elements

The numerical method is based upon approximating the body with surface elements over which the source density is assumed constant or a known function of one of the coordinates. We are only interested in axisymmetric bodies. A considerable simplification is obtained when the surface elements are chosen as shown in Figure 2.1. Because of the symmetry in the problem, this choice is evident in the axisymmetric flow where the source density is assumed constant over each element. For the cross flow, on the other hand, it is not

obvious that an optimal choice of elements has been made. It can be shown (12), however, that the source density is a cosine-function of the angle with the free cross flow direction. The source density on each element is then chosen as a constant multiplied by cos θ.

When we on each element choose a test point $\vec{x}_i$ (i=1,N where N is the total number of elements) and calculate equation(2.7) for each x_i, N algebraic equations in N unknown source strengths are obtained. This system is readily solved by iteration or inversion. The procedure is carried through for both the cross flow and the axisymmetric flow. The results are finally added to give the total solution of our problem.

The method has been used to calculate the incompressible potential flow around a cone with 10° semiapex angle. To introduce a characteristic length in the problem we have considered a conical forebody on an infinite cylinder. Calculations have been made for the following angles of attack: 0°, 5°, 10° 15°, 20°, 25° and 30°. A selection of the results is reproduced in Figure 2.2.

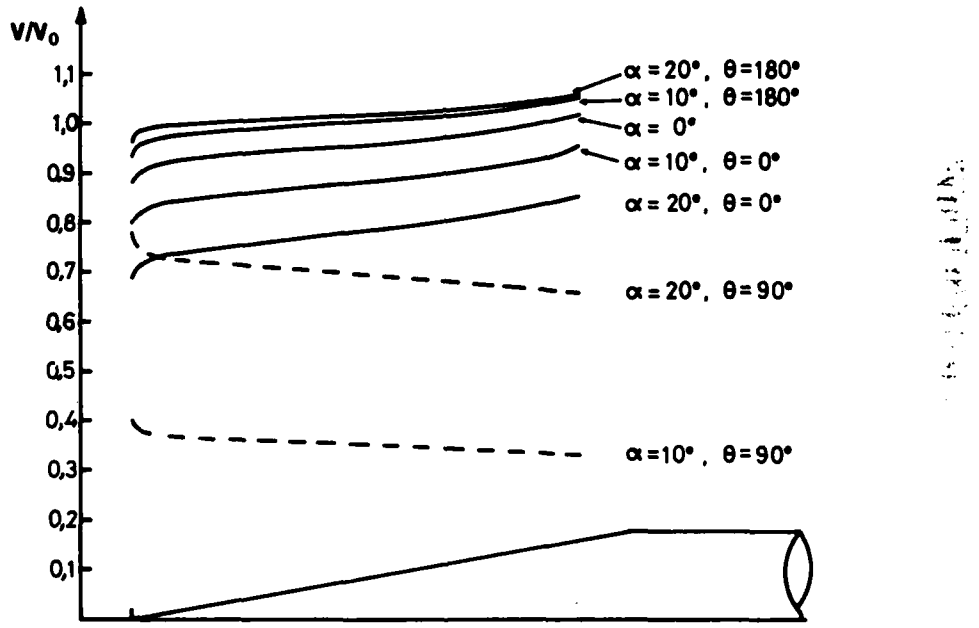

Figure 2.2 Inviscid axisymmetric and circumferential (dashed lines) velocity for various angles of attack (α) on certain generators
θ = circumferential angle from the windward side
V_0 = free stream velocity

Calculations on the same body with a spherical nose have also been performed and some of the results are found in Figure 2.3.

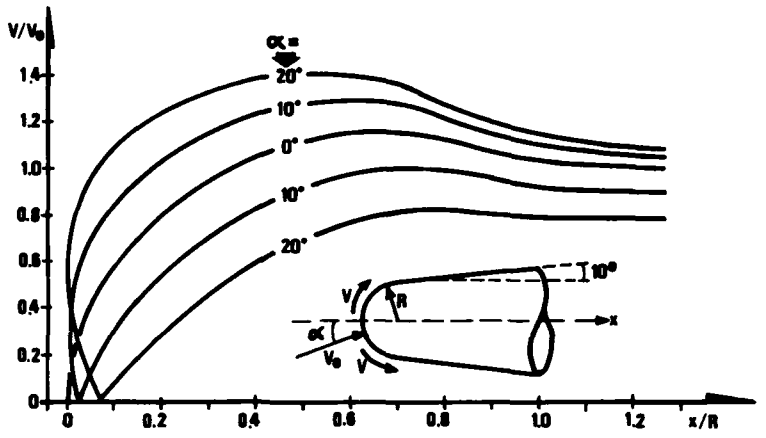

Figure 2.3 The inviscid surface flow velocity along the windward and leeward symmetry lines for various angles of attack (α)

3 THE COORDINATE SYSTEM

For various reasons which will be considered in connection with the boundary layer calculation (Chapter 4) it is advantageous to use streamline coordinates. When equipotential lines are used as the other set of coordinates, we have an orthogonal coordinate system on the body surface. The metric tensor is diagonal.

The inviscid flow velocities on a cone at several angles of attack were calculated in the previous chapter. These results are now used in streamline and potential calculations.

The equation for the streamlines on the surface is

$$\frac{U_\theta}{U_g} = \frac{r d\theta}{dx} \tag{3.1}$$

where U_θ is the circumferential velocity and U_g is the velocity in the generator direction. Furthermore, r is the local radius of the body, θ is the circumferential angle and x is the arc length along the local generator.

The calculations are initiated either from a stagnation point or from a curve orthogonal to the streamlines. The potential is given by

$$\Phi = \int_{s_0}^{s} U \, ds \tag{3.2}$$

where U is the total inviscid velocity on the surface and s is the arc length along a streamline.

The integrations are carried out by a Runge-Kutta method (14). The streamlines and equipotential lines thus obtained are used in the boundary layer calculations. Both metric coefficients and curvature parameters have to be calculated during the integration.

When the cone operates under an angle of attack, the streamlines will deviate from the windward side and coalesce at the leeward side (Figure 3.1). After a certain distance of integration the streamlines have to be reinitiated to retain the mesh size within certain limits.

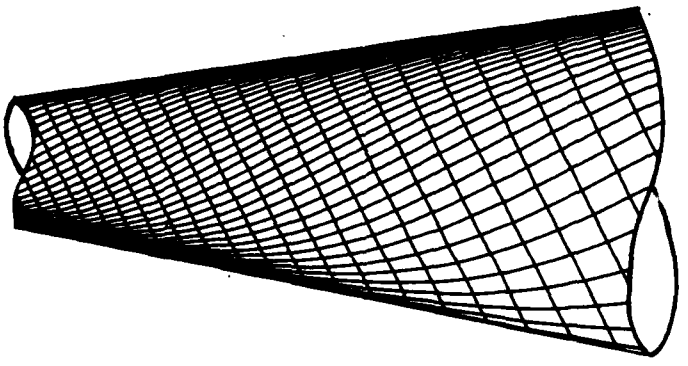

Figure 3.1 Streamlines and equipotential lines on a part of the cone at 15 degrees incidence

4 BOUNDARY LAYER CALCULATIONS

4.1 The equations

A three-dimensional, incompressible, laminar boundary layer flow is in orthogonal curvilinear coordinates given by the following equations.

Continuity:

$$\frac{1}{h_1}\frac{\partial u}{\partial \xi} + \frac{1}{h_2}\frac{\partial v}{\partial \eta} + \frac{\partial w}{\partial z} - K_1 u - K_2 v = 0 \tag{4.1a}$$

ξ-momentum:

$$\frac{u}{h_1}\frac{\partial u}{\partial \xi} + \frac{v}{h_2}\frac{\partial u}{\partial \eta} + w\frac{\partial w}{\partial z} - K_2 uv + K_1 v^2 = -\frac{1}{\rho h_1}\frac{\partial p}{\partial \xi} + \frac{\partial^2 u}{\partial z^2} \tag{4.1b}$$

η-momentum:

$$\frac{u}{h_1}\frac{\partial v}{\partial \xi} + \frac{v}{h_2}\frac{\partial v}{\partial \eta} + w\frac{\partial v}{\partial z} - K_1 uv + K_2 u^2 = -\frac{1}{\rho h_2}\frac{\partial p}{\partial \eta} + \frac{\partial^2 v}{\partial z^2} \tag{4.1c}$$

where z and w are scaled variables given by $z = \sqrt{Re}\cdot z'$ and $w = \sqrt{Re}\cdot w'$. The dimensionless lengths (ξ,η,z') and velocities (u,v,w') are derived from physical quantities by division by a reference length L and a reference velocity U_0, respectively. The metric coefficients h_1 and h_2 are functions of ξ and η. The parameters K_1 and K_2 are the geodesic curvatures of the constant ξ-curves and constant η-curves, respectively.

$$K_1 = -\frac{1}{h_1 h_2}\frac{\partial h_2}{\partial \xi}\ ,\ K_2 = -\frac{1}{h_1 h_2}\frac{\partial h_1}{\partial \eta} \tag{4.2}$$

Inviscid streamlines on the surface and curves perpendicular to them are chosen as coordinate system. When the inviscid surface-flow is potential, the second set of coordinate curves is equipotential lines.

At the outer edge of the boundary layer the momentum equations reduce to

$$\rho\frac{U}{h_1}\frac{\partial U}{\partial \xi} = -\frac{1}{h_1}\frac{\partial p}{\partial \xi} \tag{4.3b}$$

$$\rho K_2 U^2 = -\frac{1}{h_2}\frac{\partial p}{\partial \eta} \tag{4.3c}$$

where U is the inviscid surface-velocity.

The boundary layer equations can now be solved in their dimensionless coordinates ξ, η and z, but a second transformation is advantageous.

Depending on the pressure gradient, the thickness of the boundary layer will change in the streamwise direction. We know from similarity analysis (15) that a constant

outer flow will produce a boundary layer growing with the square root of the streamwise distance. When the outer flow is retarded, the boundary layer grows faster and with acceleration, it may even shrink. We shall make calculations in all these domains. Thus it is not obvious that a certain scaling in the vertical direction will reduce the computation time. When numerical tests were performed, it proved economic to introduce a new vertical coordinate

$$\zeta = f(\xi,\eta)z \quad , f(\xi,\eta) = \quad s^{-1/2} \tag{4.4}$$

where s is the streamwise distance from the attachment point. This scaling makes it possible to work with the same vertical grid-spacing throughout the entire computation.

Equations (4.3) and (4.4) inserted into (4.1) yield

Continuity:

$$\frac{1}{h_1}\left(\frac{\partial u}{\partial \xi} + \frac{\partial u}{\partial \eta}\frac{\zeta}{f}\frac{\partial f}{\partial \xi}\right) + \frac{1}{h_2}\left(\frac{\partial v}{\partial \eta} + \frac{\partial v}{\partial \zeta}\frac{\partial f}{\partial \eta}\frac{\zeta}{f}\right) + \frac{\partial w}{\partial \zeta} f - K_1 w - K_2 v = 0 \tag{4.5a}$$

ξ-momentum:

$$\frac{u}{h_1}\left(\frac{\partial u}{\partial \xi} + \frac{\zeta}{f}\frac{\partial f}{\partial \xi}\frac{\partial u}{\partial \zeta}\right) + \frac{v}{h_2}\left(\frac{\partial u}{\partial \eta} + \frac{\zeta}{f}\frac{\partial f}{\partial \eta}\frac{\partial u}{\partial \zeta}\right) + wf\frac{\partial u}{\partial \zeta} - K_2 uv + K_1 v^2 =$$

$$\frac{U}{h_1}\frac{\partial U}{\partial \xi} + f^2\frac{\partial^2 u}{\partial \zeta^2} \tag{4.5b}$$

η-momentum:

$$\frac{u}{h_1}\left(\frac{\partial v}{\partial \xi} + \frac{\zeta}{f}\frac{\partial f}{\partial \xi}\frac{\partial v}{\partial \zeta}\right) + \frac{v}{h_2}\left(\frac{\partial v}{\partial \eta} + \frac{\zeta}{f}\frac{\partial f}{\partial \eta}\frac{\partial v}{\partial \zeta}\right) + wf\frac{\partial v}{\partial \zeta} - K_1 uv + K_2 u^2 =$$

$$K_2 U^2 + f^2\frac{\partial^2 v}{\partial \zeta^2} \tag{4.5c}$$

4.2 Numerical method

When phenomena related to high angle-of-attack aerodynamics are to be investigated, the calculation of boundary layer separation is of great interest. The flow-velocity perpendicular to the inviscid streamlines (secondary flow) will then, in general, not be small, and the flow cannot be satisfactorily described by a small perturbation of a readily solvable problem. For these reasons we cannot use numerical methods based on common simplifications such as small secondary flow or small perturbations.

Hall (16) has developed a finite difference scheme which relies on neither of these simplifications. We shall, like Geissler (17), use this method in streamline coordinates.

4.3 Discretization

The computational molecule is shown in Figure 4.1. The grid sizes in the three directions are $\Delta\xi$, $\Delta\eta$ and $\Delta\zeta$ respectively. They are kept constant throughout the

computation. A suffix notation is adopted to denote position: $u_{l,m,n} = u(l\Delta\xi, m\Delta\eta, n\Delta\zeta)$.

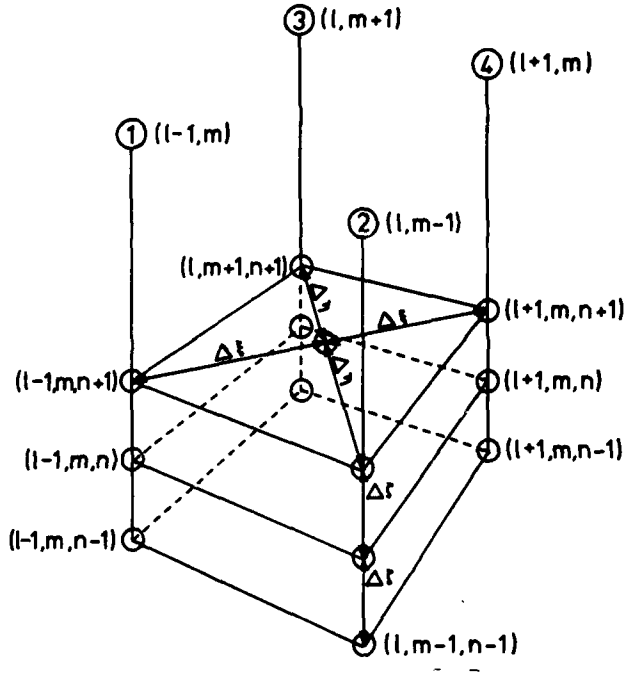

Figure 4.1 The computational molecule

The momentum equations are discretizated at the point $(l\Delta\xi, m\Delta\eta, n\Delta\zeta)$. Assuming the velocities known at $((l-1)\Delta\xi, m\Delta\eta)$, $(l\Delta\xi, (m+1)\Delta\eta)$ and $(l\Delta\xi, (m-1)\Delta\eta)$ for all n, we shall calculate the velocities at $((l+1)\Delta\xi, m\Delta\eta)$.

The finite difference approximation is given by

$$u_{l,m,n} = \frac{1}{2}[u_{l+1,m,n} + u_{l-1,m,n}] + 0(\Delta\xi^2)$$

$$\left(\frac{\partial u}{\partial \xi}\right)_{l,m,n} = \frac{1}{2\Delta\xi}[u_{l+1,m,n} - u_{l-1,m,n}] + 0(\Delta\xi^2)$$

$$\left(\frac{\partial u}{\partial \eta}\right)_{l,m,n} = \frac{1}{2\Delta\eta}[u_{l,m+1,n} - u_{l,m-1,n}] + 0(\Delta\eta^2)$$

$$\left(\frac{\partial u}{\partial \zeta}\right)_{l,m,n} = \frac{1}{4\Delta\zeta}[u_{l+1,m,n+1} - u_{l+1,m,n-1} + u_{l-1,m,n+1} - u_{l-1,m,n-1}] + 0(\Delta\xi^2 + \Delta\zeta^2)$$

$$\left(\frac{\partial^2 u}{\partial \zeta^2}\right)_{l,m,n} = \frac{1}{2(\Delta\zeta)^2}[u_{l+1,m,n+1} - 2u_{l+1,m,n} + u_{l+1,m,n-1} + u_{l-1,m,n+1} - 2u_{l-1,m,n} + u_{l-1,m,n-1}] + 0(\Delta\zeta^2 + \Delta\xi^2)$$

$$v_{l,m,n} = \frac{1}{2}[v_{l+1,m,n} + v_{l-1,m,n}] + 0(\Delta\xi^2)$$

$$\left(\frac{\partial^2 v}{\partial \zeta^2}\right)_{l,m,n} = \frac{1}{2(\Delta\zeta)^2}[v_{l+1,m,n+1} - 2v_{l+1,m,n} + v_{l+1,m,n-1} + v_{l-1,m,n+1} - 2v_{l-1,m,n} + v_{l-1,m,n-1}] + 0(\Delta\xi^2 + \Delta\zeta^2) \quad (4.6)$$

The accuracy of the discretizated equations is of second order.

We now end up with non-linear equations for the unknown velocities at ((1+1) $\Delta\xi$,m$\Delta\eta$). The equations are solved by iteration. When quadratic terms in the unknown quantities arise, we reformulate them in the following way

$$\left(u \frac{\partial u}{\partial \xi}\right)^{j+1} = u^j \left(\frac{\partial u}{\partial \xi}\right)^{j+1} + u^{j+1} \left(\frac{\partial u}{\partial \xi}\right)^j - u^j \left(\frac{\partial u}{\partial \xi}\right)^j \quad (4.7)$$

where the upper index j indicates the cycle of iteration.

When the momentum equations are discretizated by the approximations (4.6) and (4.7) we arrive at the following linear equations

$$a_n u_{l+1,m,n+1} + b_n u_{l+1,m,n} + c_n u_{l+1,m,n-1} = d_n \quad (4.8a)$$

$$a'_n v_{l+1,m,n+1} + b'_n v_{l+1,m,n} + c'_n v_{l+1,m,n-1} = d'_n \quad (4.8b)$$

The coefficients are given in Appendix A, and the quantities contained there are either known from previous calculations or boundary conditions. When velocities at station 4 (see Figure 4.1) appear in the coefficients, we use results from the previous cycle of iteration.

The discretization of the equation of continuity is performed differently. The finite difference approximation is evaluated at ($l\Delta\xi$,m$\Delta\eta$,(n−1/2)$\Delta\zeta$) as follows

$$\left(\frac{\partial w}{\partial \zeta}\right)_{l,m,n-1/2} = [w_{l,m,n} - w_{l,m,n-1}]/\Delta\zeta + 0(\Delta\zeta^2)$$

$$\left(\frac{\partial u}{\partial \xi}\right)_{l,m,n-1/2} = [u_{l+1,m,n} - u_{l-1,m,n} + u_{l+1,m,n-1} - u_{l-1,m,n-1}]/4\Delta\xi + 0(\Delta\xi^2 + \Delta\zeta^2)$$

$$\left(\frac{\partial v}{\partial \eta}\right)_{l,m,n-1/2} = [v_{l,m+1,n} - v_{l,m-1,n} + v_{l,m+1,n-1} - v_{l,m-1,n-1}]/4\Delta\eta + 0(\Delta\eta^2 + \Delta\zeta^2)$$

$$\left(\frac{\partial u}{\partial \zeta}\right)_{l,m,n-1/2} = [u_{l+1,m,n} - u_{l+1,m,n-1} + u_{l-1,m,n} - u_{l-1,m,n-1}]/2\Delta\zeta + 0(\Delta\zeta^2 + \Delta\xi^2)$$

$$\left(\frac{\partial v}{\partial \zeta}\right)_{l,m,n-1/2} = [v_{l,m+1,n} - v_{l,m+1,n-1} + v_{l,m-1,n} - v_{l,m-1,n-1}]/2\Delta\zeta + 0(\Delta\zeta^2 + \Delta\eta^2)$$

$$u_{l,m,n-1/2} = [u_{l+1,m,n} + u_{l-1,m,n} + u_{l+1,m,n-1} + u_{l-1,m,n-1}]/4 + 0(\Delta\xi^2 + \Delta\zeta^2)$$

$$v_{l,m,n-1/2} = [v_{l+1,m,n} + v_{l-1,m,n} + v_{l+1,m,n-1} + v_{l-1,m,n-1}]/4 + 0(\Delta\xi^2 + \Delta\zeta^2) \quad (4.9)$$

The equation of continuity can now be discretizated to give

$$w_{l,m,n} = w_{l,m,n-1} + \Delta\zeta\left(K_1\sqrt{s} + K_2\sqrt{s}v - \frac{\sqrt{s}}{h_1}\frac{\partial u}{\partial \xi} + \frac{\zeta}{2\sqrt{s}}\frac{\partial u}{\partial \zeta} + \frac{\zeta}{2\sqrt{s}h_2}\frac{\partial s}{\partial \eta}\frac{\partial v}{\partial \zeta} - \frac{\sqrt{s}}{h_2}\frac{\partial v}{\partial \eta}\right)_{l,m,n-1/2} \quad (4.10)$$

and when the streamwise and secondary velocity components are known, the vertical velocity can be computed successively from the bottom to the top of the boundary layer. By discretization and use of an iteration technique, the boundary layer equations have been converted to a set of coupled, linear algebraic equations.

The iteration procedure is as follows. The secondary and streamwise velocities at stations 1, 2 and 3 (see Figure 4.1) are assumed known, and we start with an extrapolation

$$u_{l+1,m,n} = u_{l,m+1,n} + u_{l,m-1,n} - u_{l-1,m,n}$$
$$v_{l+1,m,n} = v_{l,m+1,n} + v_{l,m-1,n} - v_{l-1,m,n} \qquad (4.11)$$

Equation (4.10) can now be solved for the vertical velocities. We start with the normal velocity on the surface (which is normally zero) and make a stepwise calculation up to the outer edge of the boundary layer.

The vertical velocities are now inserted in equation (4.8b) where extrapolated values (equation 4.11) are used in the coefficients. With known boundary velocities the set of equations thus obtained is solved by matrix inversion.

A similar procedure is used to solve equation (4.8a), but now the calculated secondary velocities are used in the coefficients. This completes the first cycle of iteration, and we start the second one with the just calculated velocities as input.

The results are presumably improved by each cycle, and the iteration is continued until the results of two successive cycles differ by less than a prescribed value. The iteration is then terminated and we proceed to the next station in the boundary layer where the described procedure is repeated.

4.4 The coordinate system

We shall now motivate our choice of coordinate system for boundary layer calculations. The coordinates can, in principle, be based on the body's geometry or on the inviscid streamlines. If the body is relatively simple, a geometry-oriented system may be advantageous. The metric and coefficients of curvature may then be calculated analytically. If streamline coordinates are chosen, both the coordinate system and the geometry parameters must in general be obtained by numerical integration. This calculation is a major undertaking and it must be repeated for every angle of attack considered. Yet it turns out that these extra calculations pay off in our cases.

A cone with a spherical nose will be considered. The simplest coordinate system, for which the geometrical parameters can be found analytically, is shown in Figure 4.2. With a non-zero angle of attack, the stagnation point S is displaced from the tip T, which is the origo for the body coordinates. Becase of their mathematical structure boundary layer equations have to be solved from the stagnation point, but this is impossible in these coordinates. To overcome this problem, Cebesi *et al* (18) introduce local streamline coordinates in the neighbourhood of the stagnation point. These must be calculated separately for each angle of attack and be connected with the body coordinates further downstream.

The initialization causes no geometric complications in streamline coordinates (Figure 4.2).

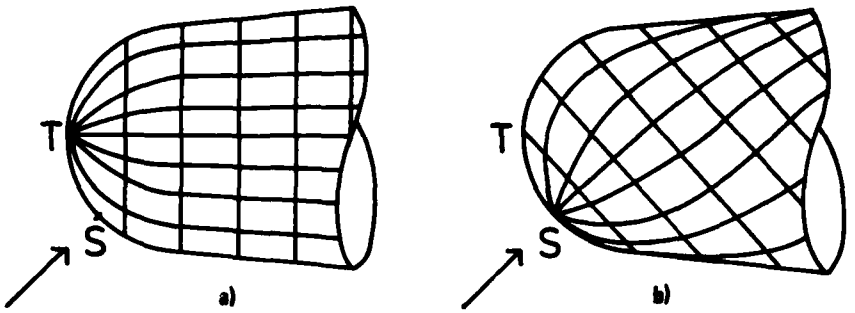

Figure 4.2 a) Body and b) streamline coordinates

The line of three-dimensional boundary layer separation on a cone at angle of attack will nearly coincide with a generator (19). In body coordinates, it is natural to choose generators as one family of coordinates. Figure 4.3a indicates a grid of coordinate curves and the line of separation. When in the calculative procedure a point A beyond the line of separation is reached, the boundary layer approximation has broken down. In Hall's numerical scheme, results at A influence the calculations at B, C, D, etc. The hatched area is therefore excluded from integration.

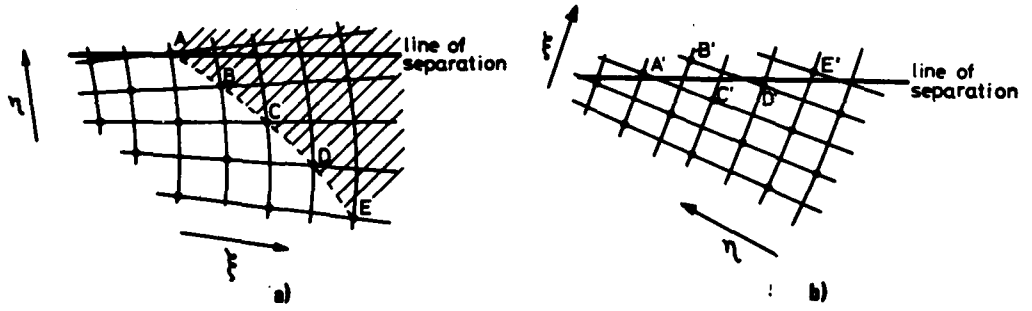

Figure 4.3 a) The line of separation in body-coordinates and b) streamline coordinates

Figure 4.3b gives a typical situation for streamline coordinates. During the process of calculation, we reach a point A′ which is beyond separation. The boundary layer calculation breaks down at this point. Calculations at B′ are abandoned, but point C′ can still be calculated. This point is upstream of separation. Results at D′ follow before a new breakdown at E′. In this way the line of separation can be traced down the cone.

The mathematical foundations for analysis of convergence and stability of numerical schemes are well-developed only for linear systems. The results from linear theory are used as guidelines in nonlinear problems. The confirmation of the validity of this method is dependent on numerical experiments.

As far as stability is concerned, we shall not perform analysis of the equations. Only Courant's stability condition (20), which is developed for linear equations, will be considered. This condition states that the finite difference domain of influence must at least include the continuum domain of influence. When only convective terms are included it yields

$$\left|\frac{v}{u}\,\frac{h_1}{h_2}\,\frac{\Delta\xi}{\Delta\eta}\right| < 1 \tag{4.12}$$

The maximum value of the secondary flow v is usually minimized when streamline coordinates are chosen. This system thus allows larger steps in the streamwise direction ($\Delta\xi$) than any system of body coordinates.

Based on these considerations, the choice of streamline coordinates is evident.

4.5 Numerical test

We shall test the numerical code by applying it to a problem with known solution. The code is developed to deal with boundary-layer flows in three dimensions. The test example should therefore have three-dimensional character.

When streamline coordinates are applied to a three-dimensional problem, there must be a component of secondary flow within the boundary layer. In applying the code, we shall mainly work with problems where the secondary flow in the lower part of the boundary layer is comparable with the streamwise velocity there. The numerical code imposes, in principle, no restriction on the magnitude of the secondary flow. A proper test example should therefore produce substantial secondary flow.

We consider incompressible flow over a flat plate with inviscid flow velocity

$$\begin{aligned} U &= 1 \\ V &= -x \end{aligned} \tag{4.13}$$

where U and V are the flow components along the x and y axes, respectively.

By inspection, symmetries are found which permit similarity simplifications. The boundary-layer problem is then reduced to two coupled ordinary differential equations. When a Runge-Kutta routine is applied, the equations can easily be solved by a shooting technique.

It should be noted that there are numerous examples where three-dimensional boundary layer equations are reduced by similarity considerations. Most of them are physically unrealistic because the inviscid flow does not satisfy the Euler equation. The chosen test example is one of the few which are dynamically possible.

Hall's numerical method will be tested against the similarity solution. Hall (16) has himself tested the method on a similar problem, but his numerical solution is more straightforward than in the present case. That is because he calculates in Cartesian coordinates where no geometric term appears. In addition to that we have performed a vertical scaling to keep the boundary layer inside the initial grid system.

A set of streamlines is used as coordinates. If we want to exploit the advantages of an orthogonal coordinate-system, we must find a second family of coordinates which is orthogonal to the streamlines. With potential outer flow, the equipotential lines would have done the job. In the test example the outer flow is rotational and we choose instead

$$\begin{aligned} \xi &= xe^{-y} \\ \eta &= y + x^2/2 \end{aligned} \tag{4.14}$$

as the new coordinates.

The geometry of this system will now be calculated.

$$\begin{aligned} ds^2 &= dx^2 + dy^2 = h_1^2\, d\xi^2 + h_2^2\, d\eta^2 \\ d\xi &= e^{-y}\, dx - x e^{-y}\, dy \\ d\eta &= dy + x\, dx \end{aligned} \tag{4.15}$$

These equations yield

$$\begin{aligned} h_1 &= \frac{e^y}{\sqrt{1+x^2}} \quad , \quad h_2 = \frac{1}{\sqrt{1+x^2}} \\ \frac{\partial x}{\partial \eta} &= \frac{x}{x^2+1} \quad , \quad \frac{\partial x}{\partial \xi} = \frac{e^y}{1+x^2} \\ \frac{\partial y}{\partial \eta} &= \frac{1}{x^2+1} \quad , \quad \frac{\partial y}{\partial \xi} = -\frac{x e^y}{1+x^2} \end{aligned} \tag{4.16}$$

From equations (4.16) we have

$$\begin{aligned} K_1 &= \frac{-1}{h_1 h_2} \frac{\partial h_2}{\partial \xi} = x(1+x^2)^{-3/2} \\ K_2 &= \frac{-1}{h_1 h_2} \frac{\partial h_1}{\partial \eta} = -(1+x^2)^{-3/2} \end{aligned} \tag{4.17}$$

The coordinate system used in the numerical integration is shown in Figure 4.4. The Runge-Kutta solution along the lines A and B was used as initial values. The results at point P were compared with the similarity solution there.

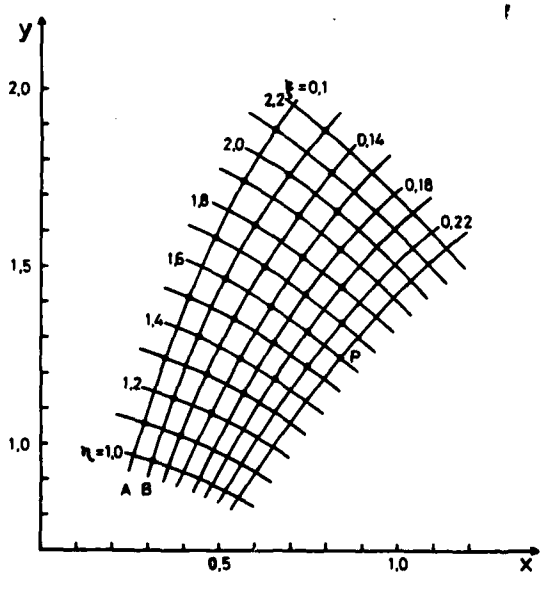

Figure 4.4 The coordinate system used in the test example

In the first test run, the mesh system in Figur 4.4 was used. We then had $\Delta\xi = 0.02$ and $\Delta\eta = 0.1$. Twenty-two points were calculated in the vertical direction. The tolerance of iteration was fixed at 10^{-4}. This means that iteration was terminated when the maximum difference between one cycle of iteration and the previous one was less than 10^{-4}.

Figure 4.5 shows the errors at point P where the calculations have proceeded six steps in the flow direction. The velocity components in the streamwise direction are within 2% of the "exact" results. The secondary component has a slightly larger relative error with a maximum deviation of 2.4%.

A reduction of the iterative tolerance to 10^{-5} produced only neglectable changes. The errors were approxi-

mately halved with 43 vertical points (Figure 4.5). For neither the streamwise nor the secondary component did they exceed 1.3%.

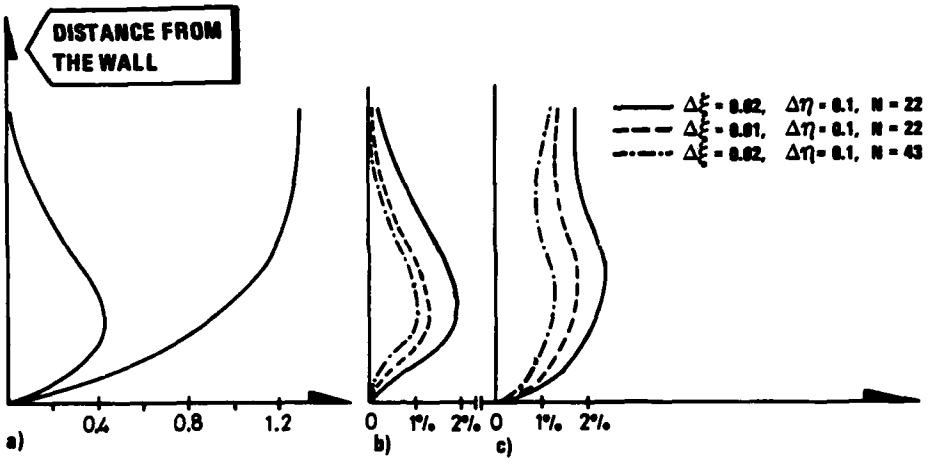

Figure 4.5 Results of finite difference calculations

a) Primary and secondary velocity profiles at P (see Figure 4.4)
b) Error in the primary profile
c) Error in the secondary profile

We then returned to 22 vertical points and reduced the step-size in the flow direction to $\Delta\xi = 0.01$. This implied 13 steps to reach P, and Figure 4.5 gives the effect on the errors. A corresponding refinement of the grid in the η-direction gave insignificant changes.

The test runs prove that the numerical solution converges to the "exact" one when the grid size is reduced. We cannot, however, draw any general conclusion about the connection between numerical error and grid size. This will depend on each particular problem. We have learned from applications, for example, that large pressure gradients require small steps.

4.6 Initiation of the boundary layer

During the discretization of the boundary layer equations (section 4.3), it turned out that as initial information we need the solution along two equipotential lines.

We shall, as previously mentioned, perform boundary layer calculations for cones at various angles of attack. To initiate the numerical procedure, a boundary layer solution for the apex region has to be known. Because there is no characteristic length for an infinite cone, this will be equivalent to a solution for the whole body. This is, however, the problem we intend to solve numerically and for which there is no known simplifying transformation.

By linearizing the potential flow and neglecting curvature, Howarth (21) has reduced the boundary layer equations in the vicinity of a stagnation point to a pair of simultaneous ordinary third-order differential equations. By using his method, the boundary layer calculations for a blunted cone can be initiated.

We therefore consider a cone with a spherical nose. For such a body the potential flow has already been calculated (Chapter 2). We first make the boundary layer calculations for axial flow. The initial profiles are calculated by Howarth's method. Just behind the line where the sphere and the cone are smoothly jointed, the boundary layer separates and further calculation is impossible (see Figure 4.6).

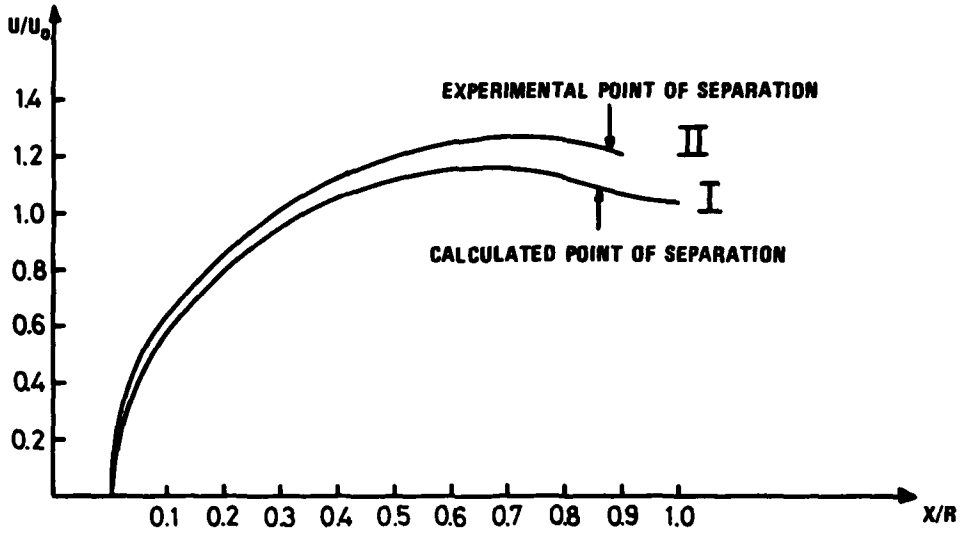

Figure 4.6 *I: The invicid surface velocity calculated for a cone with spherical nose (radius R)*
II: The experimental invicid surface velocity for a sphere (R = radius) with laminar boundary layer

We make a digression in order to compare this flow with the laminar, incompressible flow around a sphere. Figure 4.6 gives the experimental inviscid flow under the influence of the separated wake. The experimental point of separation confirms that our calculated point is reasonable.

The only parameter with dimension of length in the calculation of the flow is the radius of curvature (R) at the nose. We use this length to reduce the boundary layer equations to dimensionless form. The typical thickness of the boundary layer at the nose is

$$\delta \approx \sqrt{R} \cdot 10^{-3} \quad (\delta \text{ and R are measured in meters}). \tag{4.18}$$

One of the conditions for the validity of the boundary layer approximation is that the change of pressure through the boundary layer can be neglected. This is equivalent to having a thin boundary layer compared with the local radius of curvature of the body (15)

$$\frac{\delta}{R} \sim \frac{10^{-3}}{\sqrt{R}} \ll 1 \tag{4.19}$$

Even with 1 mm radius of curvature, relation (4.19) is satisfied.

Another condition to be met is that the continuum assumption must be valid. When the radius of curvature is reduced, the boundary layer shrinks according to equation (4.18). The continuum equations cannot be expected to hold when the boundary layer thickness is reduced to a point where it is comparable with the mean free path of the gas molecules.

We consider a radius of 1 mm. Typical thickness of the boundary layer is then 10^{-5} m. From the kinetic theory of gases (22) we have $\nu \sim \ell c$, where ν is the kinematic viscosity, ℓ is the mean free path and c is the speed of sound in the gas. For air at standard conditions this yields $\ell \sim 10^{-7}$ m. This implies that at 1 mm radius of curvature the thickness of the boundary layer is approximately one hundred mean free paths.

Even for very small dimensions, the separation must thus be real and not a result of applying the continuum theory or boundary layer approximation outside their domains of validity.

When the angle of attack exceeds ten degrees, the boundary layer stays attached on the windward side making a boundary layer calculation possible downstream along the body. We have then obtained a continuous line of separation up to which the boundary layer can be calculated (Figure 4.7).

It is known from experiments (23) that downstream of the nose-region the boundary layer is attached on the leeward side of the separation line. Hence, reattachment must take place to produce a separation bubble in the nose-region. For small and moderate angles of attack this bubble circumvents the whole body. When the body is pitched to more than ten degrees, the separation bubble is limited to the leeside of the nose (Figure 4.7). The lateral extent of the bubble is seen to be reduced when the angle of attack is increased.

We have thus worked out a method of boundary layer calculations when the cone is at high angle of attack, but we still face the initiation problem for angles of attack up to 10°.

For a pointed cone there is no known transformation which reduces the initiation problem to ordinary differential equations. When the pointed cone is at zero angle of attack, however, there exists a proper transformation due to Mangler (24).

For small angles of attack it seems reasonable that the Mangler boundary layer may work as a starting point. For moderate angles of attack, however, this seems more doubtful.

We shall now perform a numerical test of the boundary layer's sensitivity to perturbations in the initial profiles. The angle of attack is chosen to be 10°. In addition to the Mangler solution a linear profile is used initially. The difference between these two is large, but is quickly reduced when the calculations advance downstream. After ten steps the difference between the two calculations is less than one per cent in both the streamwise and secondary profile, except at the top of the boundary layer where the secondary flow velocity approaches zero.

This indicates that the effect of the initial profiles is reduced with the distance downstream. The boundary layer will be more dominated by the local pressure gradients and geometry. If the Mangler solution is chosen as the initial profile, the calculated boundary layer will be inaccurate at the first nodal points. The numerical example indicates, however, that the results improve drastically downstream.

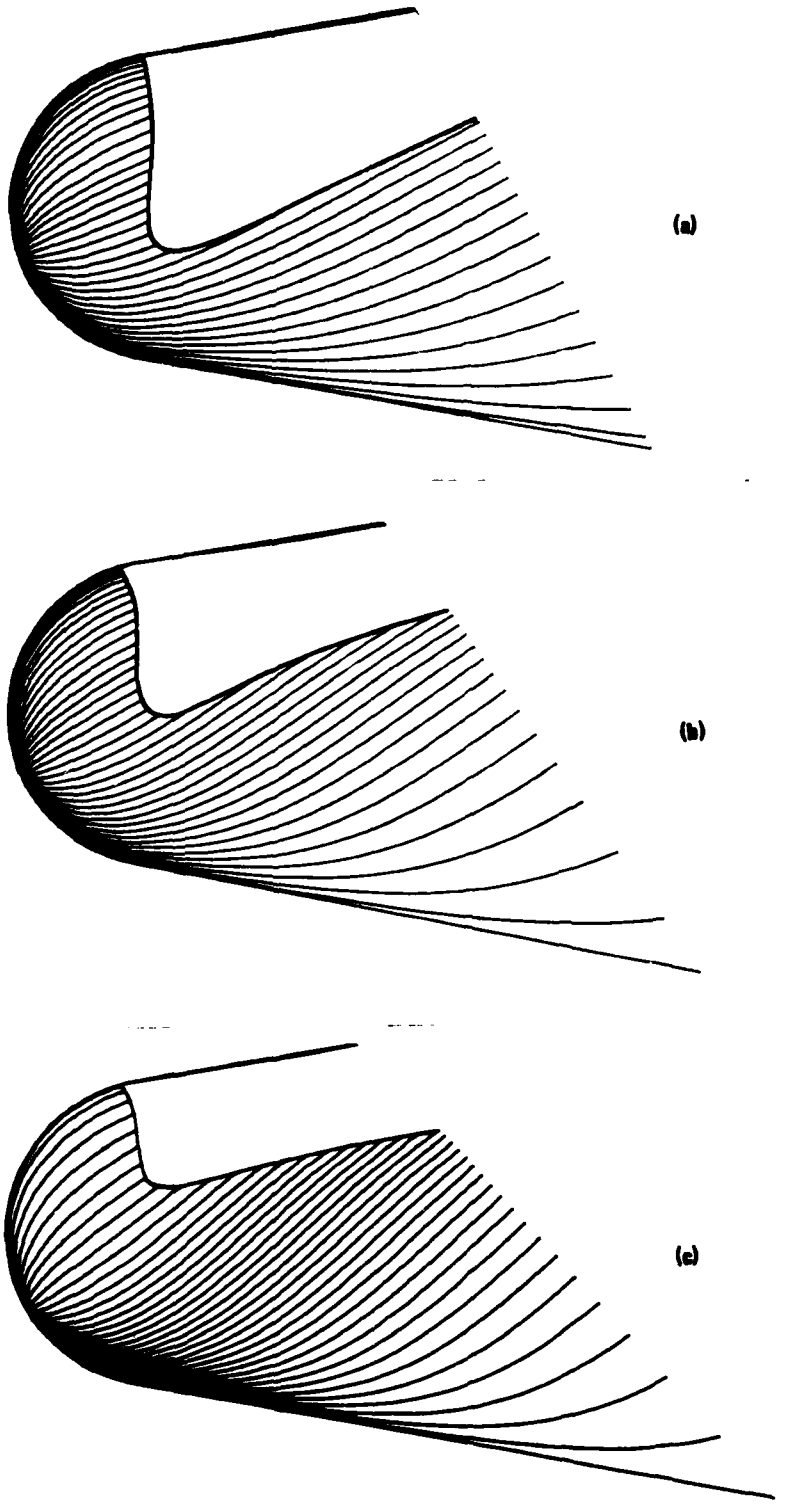

Figure 4.7 The line of separation and the inviscid streamlines on the surface of the cone with spherical nose
The angles of attack are a) 15°, b) 20° and c) 25°

This initiation is probably the best we can do for small and moderate angles of attack when blunting produces a separation bubble circumventing the nose. For the pointed cone the boundary layer theory is not valid at the apex where the potential flow is calculated to be infinite. With the proposed method we can, in principle, start the calculation arbitrarily close to the tip and reach what is believed to be a good solution as close to the tip as we wish.

4.7 Results

Equipped with the initiation methods proposed in section 4.6 we have performed boundary layer calculations based on the potential flows in Chapter 2.

There have been carried out very few detailed experiments on cones at non-zero angle of attack in the velocity domain where our assumptions are valid. The most relevant information is obtained from Rainbird *et al* (25) who have made experiments in a water tunnel. They observed the lines of separation in an area on the pointed cone where the deviation from conical symmetry is small.

We have for high angles of attack introduced blunting of the cone to make initiation of the numerical procedure possible. This means that we have to calculate down to the point where the effect of the blunting is negligible. When the distance from the blunted nose is three nose-radii, the potential flow deviates less than 1% from the flow on a similar but pointed cone. We terminate the calculations and compare with experiments when the scaled boundary layer changes insignificantly with further calculations. The scaling must be performed to compensate for the downstream growth of the boundary layer.

Rainbird *et al* have used pointed cones with semiapex angle δ of 7.5° and 12.5°, respectively. To make comparisons with our calculations (δ = 10°) we have to interpolate between results obtained for the two bodies. This is facilitated by using relative (α/δ) instead of absolute (α) incidence.

The calculations were first carried out with 5 degrees angle of attack. The boundary layer thickness increases from the windward to the leeward generator but stays attached all the way (Figure 4.8a). We further notice that the secondary flow is always in the same direction. Rainbird *et al* observe no leeside separation for the same relative incidence.

When the boundary layers are used to identify separation their form and not their physical thickness is of interest. In Figure 4.8 there is thus no vertical scale indicated.

The two-dimensional separation is a familiar and well-understood phenomenon. Under calculation, the separation is localized where the skin friction vanishes. When three-dimensional separation is considered the flow field is more complex and the definition of separation is still under discussion (11).

For the present calculation it seems natural to adopt Maskell's definitions (26). He has classified three-dimensional separation as either ordinary or singular. We shall consider the ordinary separation which results in a free shear layer. It is characterized by the property that limiting streamlines from the mainstream and the separated area meet tangentially to form what is defined as the line of separation.

In the present calculation we cannot go beyond separation. The identification of the separation line must thus be based on information obtainable at the upstream side.

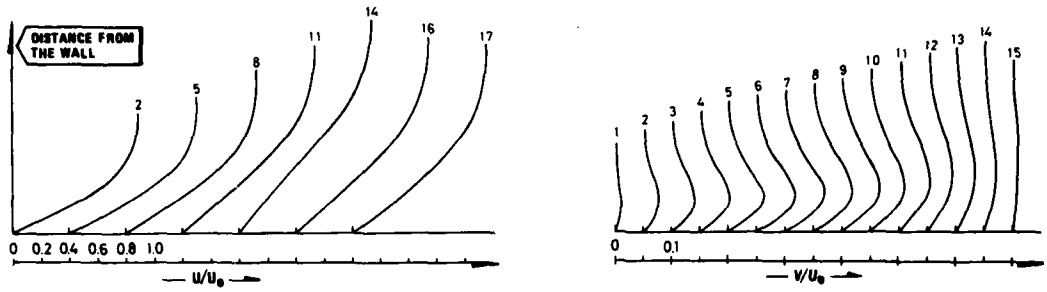

Figure 4.8a $\alpha = 5°$

θ = 1) 7.3°, 2) 21.7°, 3) 35.7°, 4) 48.8°, 5) 61.1° 6) 72.5°, 7) 83.1°, 8) 93.0°, 9) 102.2°, 10) 110.8°, 11) 118.9°, 12) 126.5°, 13) 133.8°, 14) 140.7°, 15) 147.2°, 16) 159.7°, 17) 177.1°

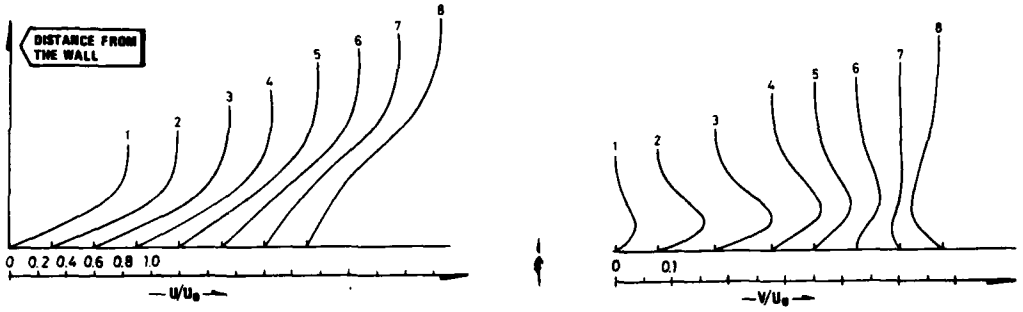

Figure 4.8b $\alpha = 10°$

θ = 1) 17.0°, 2) 47.0°, 3) 71.0°, 4) 91.2°, 5) 109.2°, 6) 117.4°, 7) 125.2°, 8) 132.6°

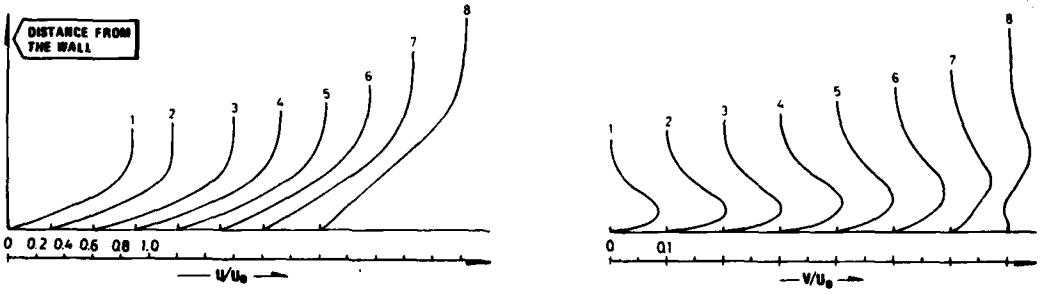

Figure 4.8c $\alpha = 15°$

θ = 1) 38.3°, 2) 55.8°, 3) 69.8°, 4) 81.4°, 5) 91.8°, 6) 101.4°, 7) 110.4°, 8) 118.8°

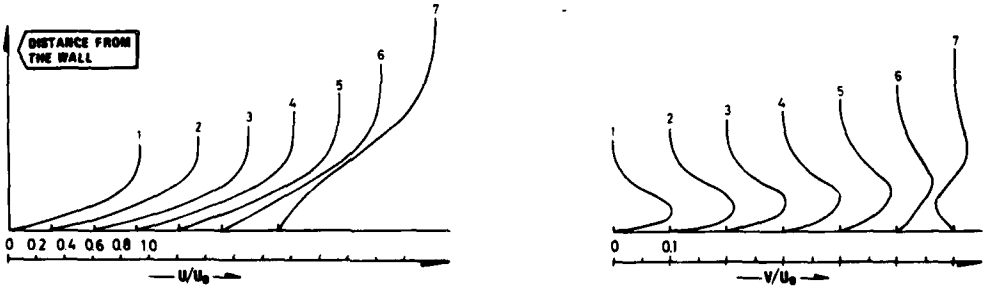

Figure 4.8d $\alpha = 20°$

θ = 1) 44.7°, 2) 65.1°, 3) 78.8°, 4) 89.8°, 5) 99.7°, 6) 109.0°, 7) 117.8°

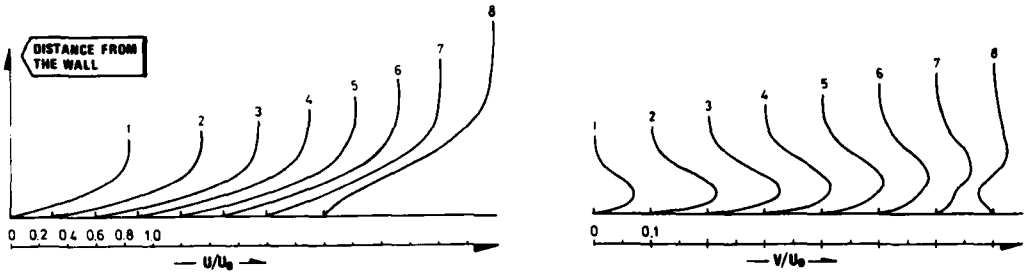

Figure 4.8e $\alpha = 25^\circ$
θ = 1) 31.6°, 2) 55.8°, 3) 68.9°, 4) 79.2°, 5) 88.5°, 6) 97.6°, 7) 106.5°, 8) 115.5°

Figure 4.8 Primary and secondary boundary layer profiles in the domain of the cone where deviation from conical symmetry is small
The profiles are given for a selection of circumferential angles θ, measured from the windward generator. It should be observed that the origos for the various curves are displaced relative to each other.

According to Maskell (26), the limiting streamlines will here coalesce to form the line of separation as their envelope curve. The central parameter will be the direction of the limiting streamlines rather than the magnitude of the skin friction which is essential in determining two-dimensional separation.

When the body is pitched to ten degrees or more, the boundary layer calculations break down on the leeside. The numerical method turns unstable. Geissler (17) claims that this feature is characteristic of separation when the calculation is effected in streamline coordinates. We want, however, to identify separation by considering limiting streamlines.

The thickness of all the calculated boundary layers increases with the distance from the windward generator (Figure 4.8). The development of the secondary flow is of particular interest. Its magnitude is seen to increase when moving away from the windward side. A maximum is reached before a more complex profile develops. The inner part of the boundary layer changes direction to form an S-shaped profile. Under these conditons the limiting streamlines approach each other in the way assumed in the separation criteria. The exact location of separation is found by extrapolating to the point where the limiting streamlines coincide with a generator. The skin friction is small but non-zero here.

When approaching this special generator, the boundary layer grows rapidly, indicating that the main flow is turned away from the surface. We have thus identified a line which satisfies our intuitive conceptions of separation as well as Maskell's formal definition.

Figure 4.9 gives a comparison of observed and calculated position of separation. For a relative incidence of 2.4 the two positions coincide exactly. At lower incidence the separation is predicted to take place too early. At higher angles we have the opposite trend.

There has been included no upstream effect of the separated flow, but this is seen to be of less importance here than in, for example, two-dimensional separation on a sphere (27).

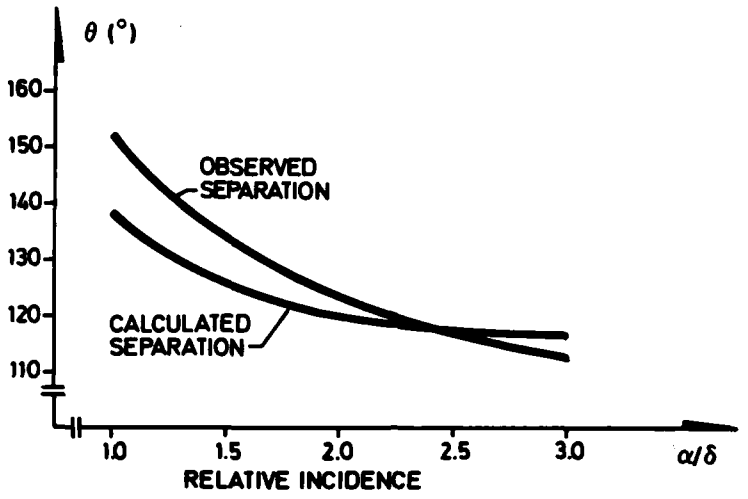

Figure 4.9 Comparison of observed (25) and calculated position of separation as function of relative incidence

5 A MODEL OF THE SEPARATED FLOW

5.1 The method

The inviscid and incompressible flow around a cone at various angles of attack was calculated in Chapter 2. These results were then used in the boundary layer calculations of Chapter 4. The calculations broke down when the line of separation was reached. We now intend to carry the calculations beyond this line. It seems further reasonable, having obtained a first approximation of the separation line, to attempt to improve on it systematically by including the wake. We therefore need a model of the separated flow.

The boundary layer leaving the surface at the separation line can be modelled by a vortex sheet springing from the surface of the body. When this sheet is linked to a wake model, the boundary layer in the resulting external flow can be calculated and a new separation line found. This iteration procedure may be followed to its eventual convergence.

The mathematical problem is surmountable if slender body theory is applied. This is shown to be, under certain conditions, a consistent first order approximation to the fundamental equations (28). These conditions are that the stream is isentropic (no strong shock), the body is slender and its angle of attack is small. The theory is thus based on the assumption that the body induces small perturbations on the flow. The angles of attack, for which leeside separation occurs, are not in this context small, and the cone perturbs the flow significantly. The conditions on which the slender body simplifications are based are thus not met and the application of the method is questionable.

The prime argument for the validity of the slender body method rests on its ultimate success. The flow fields obtained, usually by visualization techniques, are similar to the results calculated by for example Angelucci (9).

We shall use a modified version of Angelucci's method.

The flow separates from the body-surface along a three-dimensional separation line. The boundary layer is converted to a vortex sheet which rolls up into a region of distributed circulation. Rotation is therefore present not only in the boundary layer and the wake downstream of the body, but also in the external field which surrounds it.

The slender body theory used here is called the *cross-flow analogy*. It is different from the standard version which can be applied to attached flow only. The time has to be included when the flow separates on the leeside and we intend to model the wake. The calculations are made on an unsteady two-dimensional geometry. This is a major simplification compared with the original three-dimensional flow. It is in fact the best we can do with the available computer resources.

The essence of the technique is to introduce new coordinates. We make the following transformations

$$\begin{aligned} x &= \hat{x} - U_0 \cos\alpha \cdot t \\ y &= \hat{y} \\ z &= \hat{z} \end{aligned} \qquad (5.1)$$

where $\hat{x}$, $\hat{y}$ and $\hat{z}$ are coordinates linked to the body. U_0 is the velocity of the body and t is the time. The flow is now considered in the plane x=0, see Figure 5.1. In this plane the flow field is that induced by a circular cylinder of time-dependent radius (correlated with the thickness distribution of the body) in a uniform free stream of velocity $V = U_0 \sin \alpha$.

Vorticity is fed into the flow from the point of separation. There have been made several attempts to model the separated flow by a concentrated vortex core and a feeding vortex sheet (11).

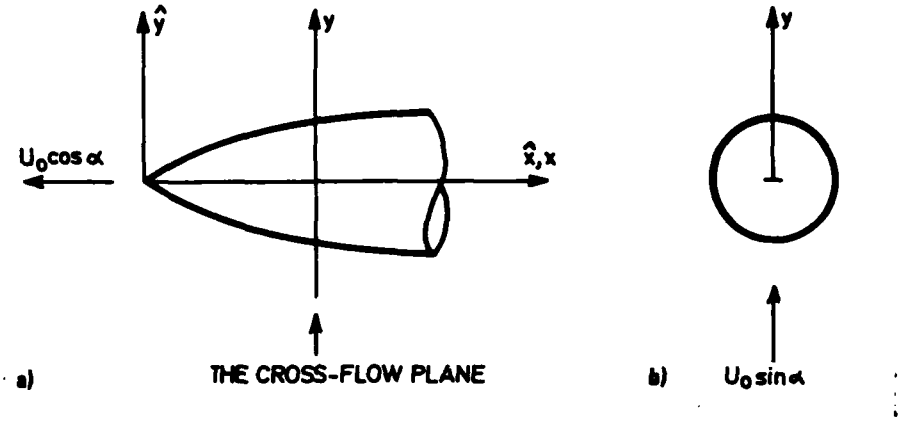

Figure 5.1 a) The coordinate transformation and b) the body in the cross-flow plane

In the present study the vortex sheet is represented by a chain of discrete vortices (29). Each of these is introduced in the flow close to the point of separation and their subsequent positions are computed step-by-step from the induced velocities on the vortices. This model allows the vortex sheet to roll up freely without the unphysical restriction of concentrated vortex cores.

The Kutta-condition used is different from that chosen by Angelucci. To establish this we have to investigate the vortex sheet close to the line of separation. Smith (30) has, by simple arguments, shown that the vortex sheet must leave the body tangentially. The flow is shown qualitatively in Figure 5.2.

With the sheet tangential to the wall we can distinguish between an upstream and a downstream side. On the downstream side of the separation line, the inviscid streamlines are nearly parallel to the separation line. From the upstream side, however, the inviscid streamlines on the wall cross the separation line and continue on the vortex sheet. The limiting streamlines of the viscous flow deviate inwards from the curved inviscid streamlines, approach the separation line but do not cross it. On the downstream side, a nearly parallel flow is envisaged in which the skin-friction lines on the wall and the inviscid streamlines are essentially parallel (only the inviscid lines are shown in Figure 5.2).

This implies that the inviscid surface velocity in the two-dimensional model must be discontinuous at the separation point.

For simplicity of calculation the vortex sheet is replaced by a chain of vortices. Close to the point of separation, however, a linear part of the sheet is retained. The procedure of calculation is as follows.

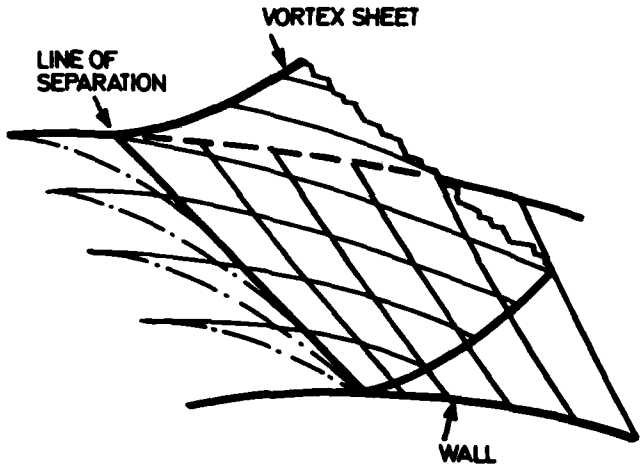

Figure 5.2 Schematic illustration of a three-dimensional separation with inviscid streamlines (solid lines) and limiting streamlines (chain lines)

On the basis of local induced velocities at the vortices at time t, their positions at t+ Δt are calculated. In the interval Δt more vorticity is fed into the wake. This additional vorticity is represented by a linear vortex sheet springing from the point of separation. The sheet is replaced by a concentrated vortex before the next step of calculation. This one is given the same total vorticity as the vortex sheet and is positioned at the centre of the sheet.

The two-dimensional Kutta-condition can now be expressed as

$$\begin{aligned} &\lim U_s > 0 \qquad \text{from the upstream side} \\ &\lim U_s = 0 \qquad \text{from the downstream side} \end{aligned} \tag{5.2}$$

where U_s is the inviscid two-dimensional surface velocity. From this we see that all two-dimensional vorticity is fed into the wake from the upstream boundary layer. The Kutta-condition is met in the calculations by adjusting the position of the linear vortex sheet. Its inner end is located a distance ϵ radially outside the separation point and it is directed towards the latest emerged vortex. The length of the vortex sheet is chosen to be 75% of the distance to this vortex. The vorticity is assumed uniform over the sheet.

The sheet will induce singular velocity at its end points (31). This is physically unrealistic. We are only interested in the surface flow and shall see that the model will give realistic conditions there.

5.2 The vortex sheet

The complex velocity potential of a vortex sheet outside a circular body of radius r_0 can be expressed as (32)

$$\Phi(\sigma) = -\frac{i}{2\pi}\int_{s_\epsilon}^{s_A}\gamma(s)\ln\left[\frac{\sigma-\sigma_i}{\sigma-r_0^2/\bar{\sigma}_i}\right]ds \tag{5.3}$$

where we, to preserve the boundary condition of no cross flow on the body surface, have included the image vortex sheet. The integration variable s is the length along the sheet and $\gamma(s)$ gives the circulation per unit length.

We assume that the sheet is linear and of uniform circulation. Thus

$$\begin{aligned} \gamma(s) &= k \\ ds &= d\sigma_i e^{-i\varphi_s} \end{aligned} \tag{5.4}$$

where ϕ_s is the angle between the sheet's direction and the real axis.

The velocity in the stream is obtained by differentiating the complex velocity potential

$$\bar{w} = u - iv = \frac{d\Phi}{d\bar{\sigma}} = -\frac{ik}{2\pi} e^{-i\varphi_s} \int_{\sigma_\epsilon}^{\sigma_A} \frac{d\sigma_i}{\sigma - \sigma_i} + \frac{ik}{2\pi} e^{i\varphi_s} \int_{\bar{\sigma}_\epsilon}^{\bar{\sigma}_A} \frac{d\bar{\sigma}_i}{\sigma - r_0^2/\bar{\sigma}_i} = \frac{ik}{2\pi} e^{-i\varphi_s} \ln\left[\frac{\sigma - \sigma_A}{\sigma - \sigma_\epsilon}\right]$$

$$+ \frac{ik}{2\pi} e^{i\varphi_s} \left(\frac{r_0^2}{\sigma^2} \ln\left[\frac{\sigma\bar{\sigma}_A - r_0^2}{\sigma\bar{\sigma}_\epsilon - r_0^2}\right] + \frac{\bar{\sigma}_A}{\sigma} - \frac{\bar{\sigma}_\epsilon}{\sigma}\right) \qquad (5.5)$$

which after a tedious but straightforward manipulation (Appendix B) gives the surface velocity in explicit form.

The surface velocity induced by the straight uniform vortex sheet and its image sheet will now be examined. We choose unit body radius and sheet strength. The sheet's length is 0.2 and $\epsilon = 0.001$.

Figure 5.3 gives the results for three different angles between the radius vector at the point of separation and the direction of the vortex sheet. The position of the vortex sheet will later be adjusted so as to meet the Kutta-condition which requires that the two-dimensional velocity is discontinuous at the separation point.

It may be argued that the velocity curves, though steep at the separation point, are still continuous. Our calculations are fundamentally based on the boundary layer approximation and this one will break down in the separation region. If we try to calculate the flow there, we shall go beyond the theory's regime of validity. Within the limitations of the theory the sheet's contribution to the surface velocity can be regarded as discontinuous.

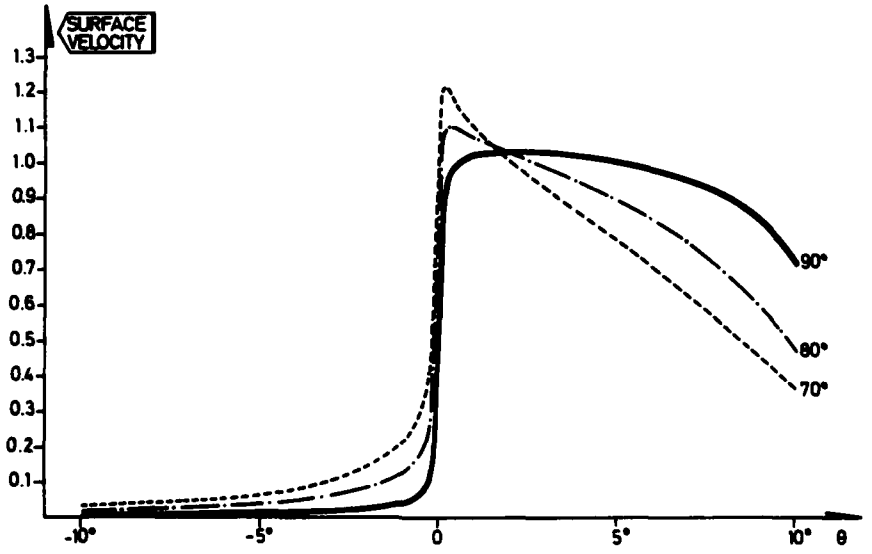

Figure 5.3 The two-dimensional surface velocity induced by a straight uniform vortex sheet at various angles with the radius vector at separation
θ is the circumferential angle from the point of separation

We see in Figure 5.3 that the upstream contribution from the sheet decreases when the sheet approaches the surface. This is consistent with what is expected. At the point of separation the boundary layer leaves the surface and continues as a vortex sheet. When the sheet is abruptly turned away from the surface, the upstream effect of the separation will be larger than with a vortex sheet close to the body.

5.3 The wake

In the slender body approximation the calculation of the wake is reduced to solving the Poisson equation in a plane which is penetrated by the cone, see Figure 5.1. At $t = t_1$ ($\dot{x} = \dot{x}_1$) the cone is represented by a circle of radius r_1 ($= \dot{x}_1 \operatorname{tg} \delta$, where δ is the semiapex angle) in the complex plane $\sigma = \zeta + i\eta$. The circular cone is equivalent to an expanding circular cylinder and the complex stream potential without vortices (uniform flow with source and doublet at origo) is (31)

$$\Phi_1(\sigma) = \frac{U_0 \cos\alpha \cdot \operatorname{tg}\delta}{r_0} \ln\sigma - iU_0 \sin\alpha \cdot (\sigma - \frac{r_0^2}{\sigma}) \tag{5.6}$$

We have already calculated the potential induced by the vortex sheet close to the point of separation

$$\Phi_2(\sigma) = \frac{-ik}{2\pi} \int_{s_\epsilon}^{s_A} \ln(\frac{\sigma - \sigma_i}{\sigma - r_0^2/\sigma_i})\, ds \tag{5.7}$$

Each of the discrete vortices in the wake contribute with

$$\Phi_3(\sigma) = -\frac{i}{2\pi} \Gamma_i \ln(\frac{\sigma - \sigma_v}{\sigma - r_0^2/\sigma_v}) \tag{5.8}$$

where Γ_i is the strength of a vortex at σ_v.

Because of the linearity of Poisson's equation the various potentials can be added to give the total potential for the flow.

There is made no assumption about symmetry. The vortices and the two vortex sheets do not have to be symmetrical about the imaginary axis, and this opens possibilities for investigating asymmetric effects.

The vortices are introduced as point vortices, but they will not retain this structure. The vorticity will be diffused.

Convection and diffusion of vorticity are given by Helmholtz equation (31)

$$\frac{D\vec{\omega}}{Dt} = (\vec{\omega} \cdot \nabla)\vec{V} + \nu \nabla^2 \vec{\omega} \tag{5.9}$$

$$\omega = \operatorname{curl} \vec{V}$$

When we neglect convection in our two-dimensional model, equation (5.9) reduces to

$$\frac{\partial \omega}{\partial t} = \nu[\frac{\partial^2 \omega}{\partial r^2} + \frac{1}{r}\frac{\partial \omega}{\partial r}] \tag{5.10a}$$

and we impose the initial condition

$$\omega = \frac{\Gamma_i}{2\pi} \delta(r) \qquad \text{at } t = 0 \tag{5.10b}$$

The solution of equation (5.10) is

$$\omega(r,t) = \frac{\Gamma_i}{4\pi} \frac{1}{\nu} e^{-r^2/4t\nu} \tag{5.11}$$

with the induced velocity distribution

$$u = \frac{1}{2r}\int_0^{2\pi}\int_0^{r}\omega r\,dr\,d\theta = \frac{\Gamma_i}{2\pi r}\left(1-e^{-r^2/4\nu}\right) \tag{5.12}$$

The total vorticity is constant but with time it is spread over an increasing area. This effect is included for two reasons. The vortices in the wake will interact, and if two of them should get close together they will introduce abnormal velocities on each other. When a vortex gets close to the body's surface, a local unphysical peak in pressure distribution will result. These effects will be damped by diffusion.

The vortex flux in a two-dimensional boundary layer will now be calculated. The vorticity is given by

$$\omega = \frac{\partial u}{\partial y} - \frac{\partial v}{\partial x} \tag{5.13}$$

but the vertical velocity v can be neglected in the boundary layer. The total flux of vorticity is then

$$\int_0^{\delta} u\omega\,dy = \int_0^{\delta} u\,\frac{\partial u}{\partial y}\,dy = U_s^2/2 \tag{5.14}$$

where δ is the thickness of the boundary layer. Thus, it turns out that in a two-dimensional boundary layer the total vorticity flux is given by the inviscid surface velocity. The actual boundary layer profile is of no consequence. We have previously concluded that the streamlines on the downstream side of separation are parallel to the separation line. This implies that the downstream boundary layer does not contribute to the two-dimensional vorticity fed into the wake. All vorticity originates from the upstream side.

The first order primary separation line was calculated in Chapter 4. To the same order of accuracy we know the inviscid velocity at separation and by equation (5.14) we have the flux of vorticity fed into the wake.

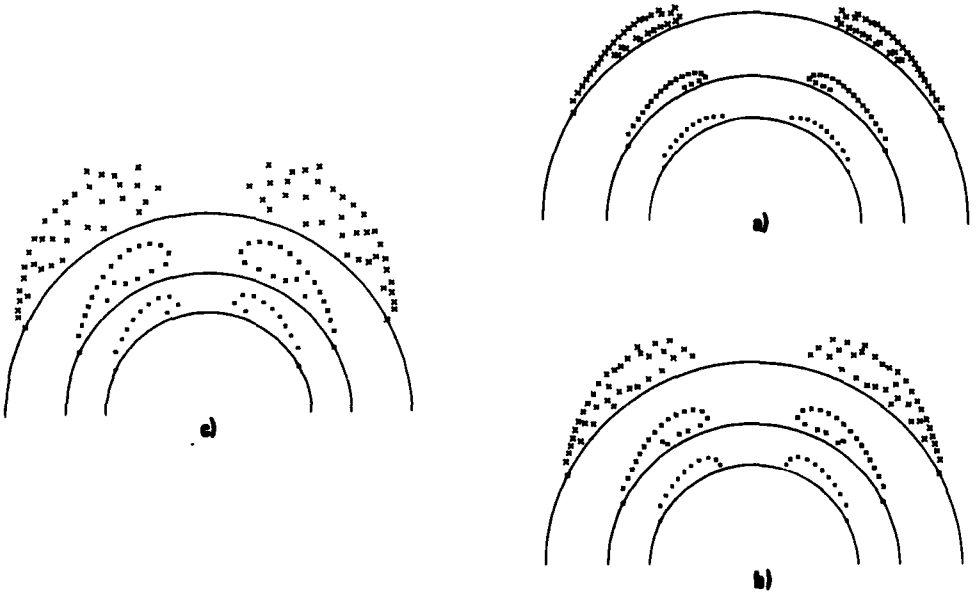

Figure 5.4 The calculated development of the wake downstream along the body
α is the angle of attack
a) $\alpha = 15^\circ$, b) $\alpha = 20^\circ$, c) $\alpha = 25^\circ$

The calculation of the wake flow is initiated with a linear vortex sheet tangential to the body. The length of the sheet is $U_s \Delta t$. U_s is the two-dimensional inviscid surface velocity at separation and Δt is the time step. The distance ϵ from the surface is adjusted so as to meet the Kutta-condition. The further calculation is as described previously.

We have made calculations of the wake for the cone at 15, 20 and 25 degrees of incidence, respectively. Figure 5.4 shows how the wakes develop in time (distance from apex). The cross flow ($U_0 \cdot \sin\alpha$) convects the vortices downstream but the circulation of the vortices opposes this effect and the vortices gather in two limited areas at the leeside of the body. This is qualitatively in agreement with flow vizualisations (3,4). They confirm that the vorticity is distributed over certain areas rather than accumulated in one concentrated vortex at each side, as is often assumed in simulations (33,34). It is also in correspondence with experiments that the vortices are squeezed down to the surface when the angle of incidence is reduced. At 20 degrees of incidence and even more pronounced at 25 degrees, the typical feeding sheet is lost. This is not in agreement with observations and we shall return to this point in Chapter 7.

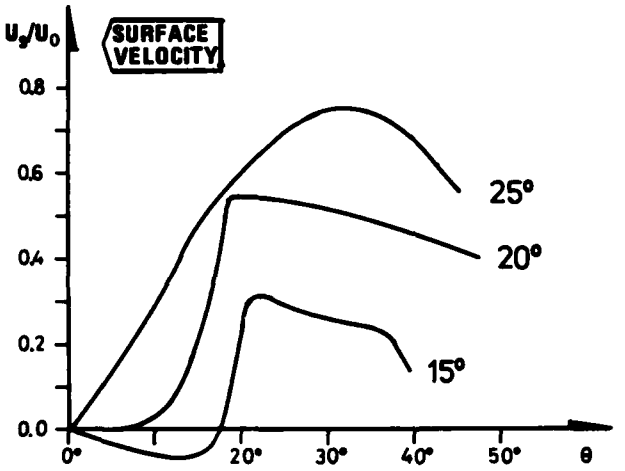

Figure 5.5 The calculated induced two-dimensional surface velocity on the cone
The angles of attack are 15, 20 and 25 degrees, respectively. θ is the circumferential angle measured from the leeside generator

The calculations are run up to the point where the time-average surface velocity is essentially stationary. We have then reached approximative conical symmetry which is reported to exist(19).

The induced surface velocities are reproduced in Figure 5.5 after a time-averaging of the curves. Even though diffusion is included to reduce the short-range effect of the vortices, they produce unphysical local variations on the surface. A time-averaging after the approximate conical symmetry is reached gives curves without abnormal peaks.

5.4 Secondary separation

When a slender rotational body is pitched to an angle where leeside separation takes place, several lines of separation are observed (19,35). The primary line is already calculated (Chapter 4) and we shall now deal with the secondary line of separation.

Figure 5.5 gives the circumferential surface velocities calculated with the two-dimensional unsteady model. Combined with the axial flow they give the total surface velocities. This flow will no longer be irrotational and there are no equipotential lines available as coordinates. We therefore have to integrate lines normal to the streamlines to obtain the second family of coordinates.

When the angle of attack α is 15°, the attachment line falls along a generator with the angle $\theta = 17.5°$ from the leeside symmetry line. From this generator the inviscid streamlines deviate in both windward and leeward directions.

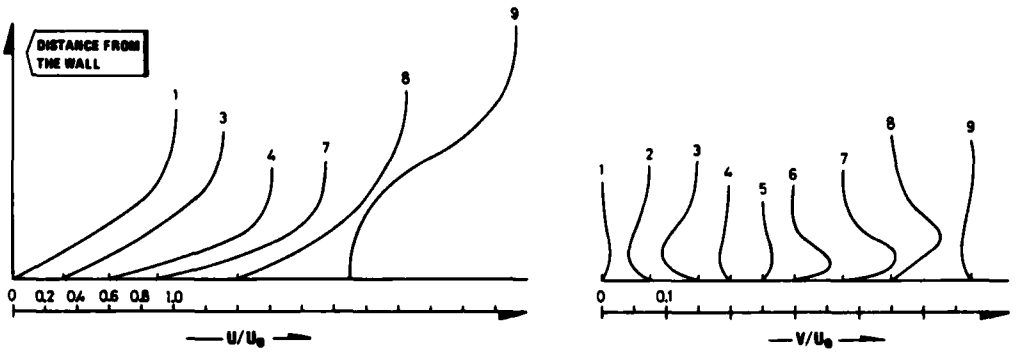

Figure 5.6a $\alpha = 15°$
θ = 1) 9,57°, 2) 13.99°, 3) 15.13°, 4) 16.37°, 5) 18.05°, 6) 19.21°, 7) 21.18°, 8) 22.69°, 9) 23.43°

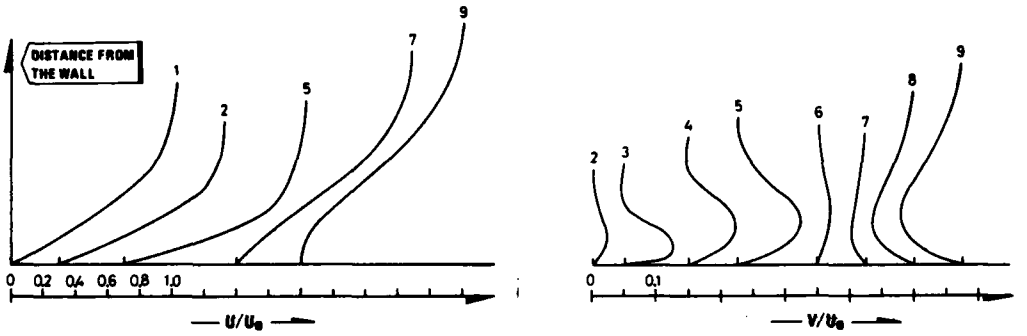

Figure 5.6b $\alpha = 20°$
θ = 1) 6.23°, 2) 12.03°, 3) 18.75°, 4) 23.16°, 5) 25.88°, 6) 29.89°, 7) 37.61°, 8) 45.06°, 9) 52.16°

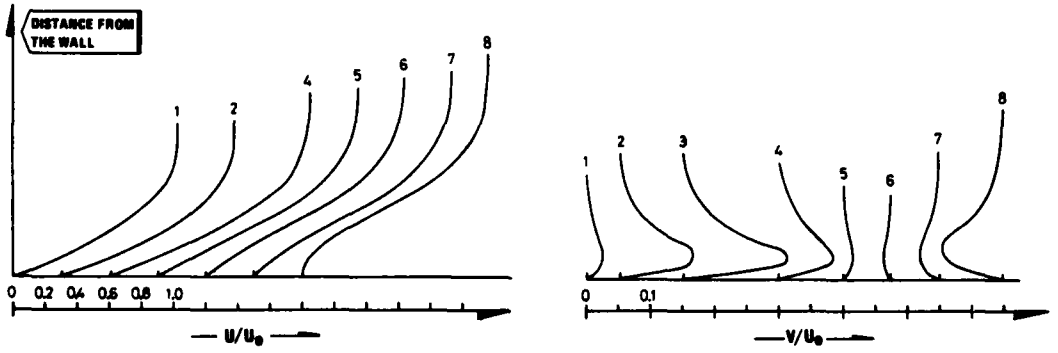

Figure 5.6c $\alpha = 25°$
θ = 1) 2.24°, 2) 11.1°, 3) 19.7°, 4) 27.9°, 5) 33.6°, 6) 35.9°, 7) 37.56°, 8) 41.5°

Figure 5.6 ***Primary and secondary boundary layer profiles on the leeside of the cone***
The profiles are given for a selection of circumferential angles θ, measured from the leeward generator. It should be observed that the origos for the various curves are displaced relative to each other.

When the body is pitched to higher angles, the line of attachment moves towards the leeward generator and they coalesce at $\alpha = 20°$.

The inviscid surface flow is now used as input for boundary-layer calculations. The results for $\alpha = 15°$ are given in Figure 5.6a. The boundary layer between the attachment line and the leeward generator is attached. At the other side of the attachment line the boundary layer develops more dramatically. Both the circumferential and total velocity increase rapidly, causing the boundary layer to shrink. The curvature of the inviscid streamlines produces substantial secondary flow in the boundary layer. The pressure gradient turns unfavourable at $\theta = 21.5°$ and the boundary layer starts growing before it eventually separates at $\theta = 23.5°$.

At $\alpha = 20°$ the boundary layer develops smoothly from the leeside generator to the domain with rapid acceleration (Figure 5.6b). The boundary layer is then compressed and a substantial secondary flow emerges. The pressure gradient is adverse from $\theta = 19°$. First it is very weak but is increases slowly as we move windward.

When calculating the primary separation we found that separation occurred in connection with reversal of the secondary flow direction. It is not so for the present flow. The direction of secondary flow is reversed at $\theta = 32°$. The boundary layer remains attached but shows signs of incipient separation over a substantial distance downstream of this point. The imposed pressure gradient is close to the limit of what the boundary layer can resist without separation. Small perturbations in the vortex-induced crossflow may displace the line of separation considerably.

At 25° the circumferential velocity increases with the distance from the leeside generator and reaches a maximum at $\theta = 31°$. The pressure gradient is adverse from this point on. Neither will the flow separate here when the secondary flow's direction is reversed (Figure 5.6c). The separation takes place at $\theta = 42°$.

We have integrated the inviscid and limiting streamlines. The results are reproduced in Figure 5.7.

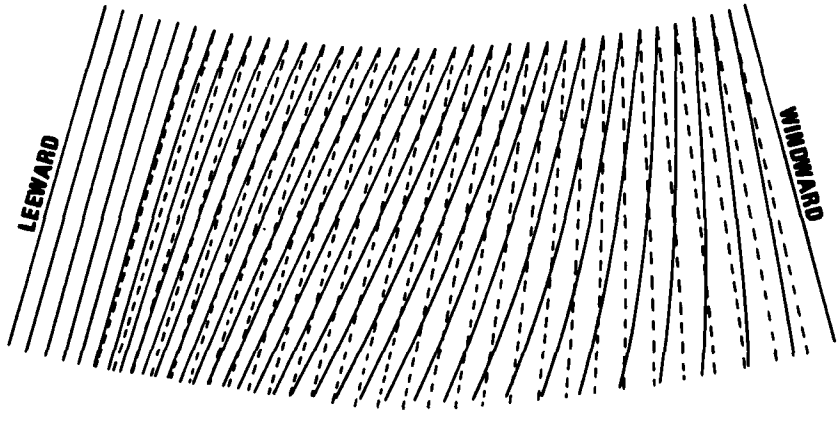

Figure 5.7a $\alpha = 5°$

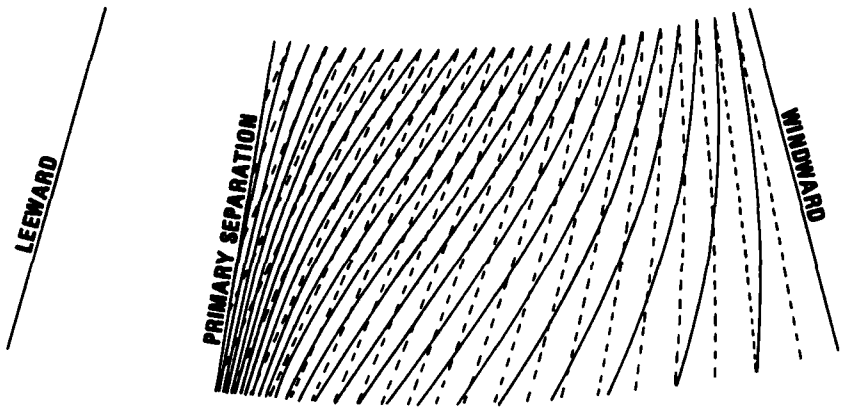

Figure 5.7b $\alpha = 10°$

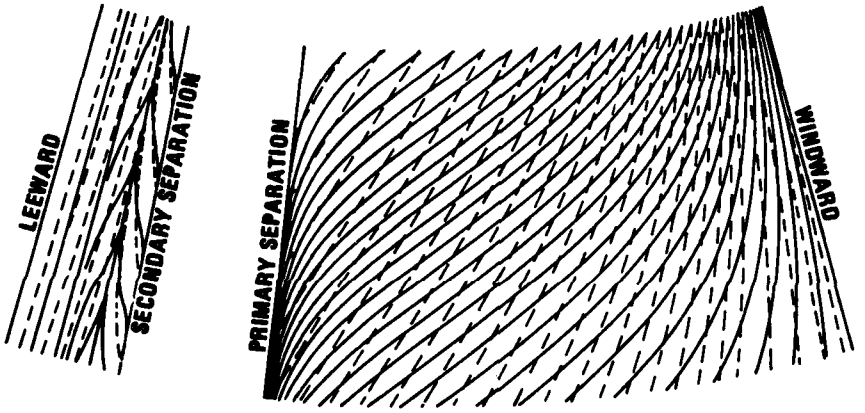

Figure 5.7c $\alpha = 15°$

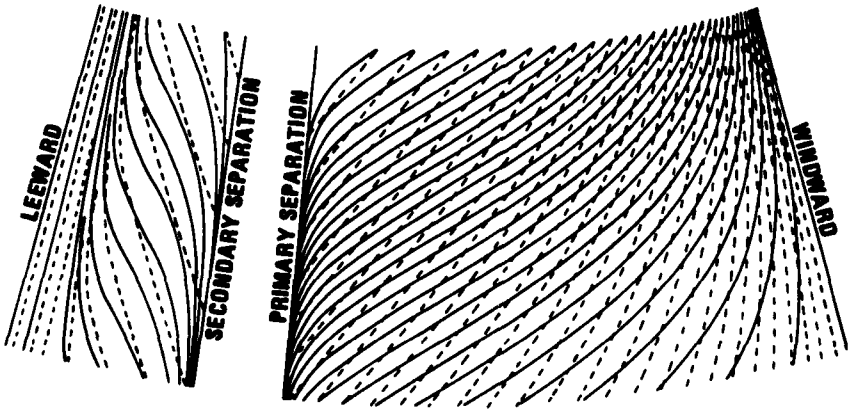

Figure 5.7d $\alpha = 20°$

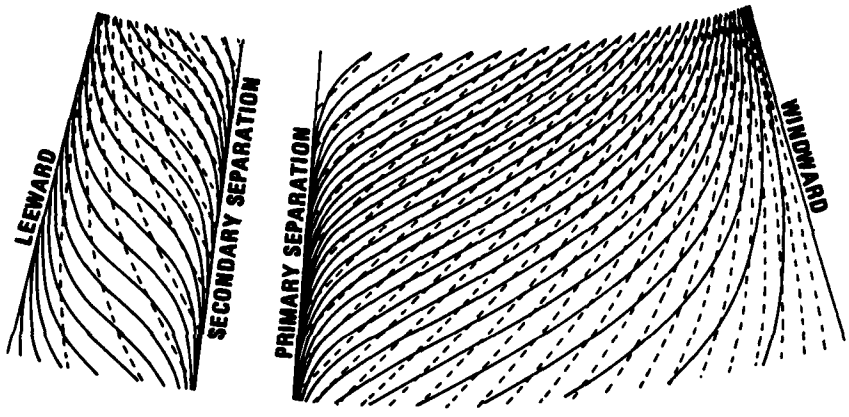

Figure 5.7e $\alpha = 25°$

Figure 5.7 The calculated inviscid (solid lines) and limiting streamlines (dashed lines) on the unwrapped cone surface at various angles of attack

The calculated lines of secondary separation are not in agreement with the experimental results of Rainbird *et al* (25). They report the locations to be nearly independent of the angle of attack. For the present cone the lines of secondary separation will coincide with a generator approximately 25° from the leeside symmetry line.

We shall return to this point in Chapter 7 where these first order results are improved in a second cycle of iteration.

6 STREAMWISE-DIRECTED VORTICES

It may be interesting to investigate whether certain phenomena which are known to occur in boundary layers will contribute to the observed asymmetric forces.

We have hitherto made all boundary-layer calculations under the assumption that they are stable and laminar, but it is well known that under certain conditions the boundary layer will be unstable and undergo transition from a laminar to a turbulent state. This is known to have a substantial effect on the location of separation (27).

It seems sensible to classify boundary-layer instability as:

- Dynamic (Taylor-Görtler) instability
- Viscous (Tollmien-Schlichting) instability
- Inflectional instability

Dynamic instability is observed in a boundary layer flow over concave surfaces where the velocity increases in the direction towards the centre of curvature.

When *viscous instability* is active, energy is by viscosity transferred from the mean flow to the disturbances. The instability of the laminar flow over a flat plate (Blasius flow) is of this type.

Inflectional instability is found when the boundary layer profile contains a point of inflection. In two-dimensional stream this typical profile appears at an adverse pressure gradient. That often implies that we are close to separation. For three-dimensional stream, inflectional profiles may occur even in regions with favourable pressure gradients. This type of instability is more effective than the viscous type when transition to turbulence is concerned.

Boltz *et al* (36) have made an experimental study of the transitional properties of the boundary layer on a swept wing. For certain configurations they found that a slight increase in Reynold's number resulted in a large forward movement of the point of transition. Flow-visualization studies showed that this substantial change of the flow was immediately preceded by the presence of streamwise-directed vortices in the boundary layer. This strongly indicates that the premature transition is caused by stationary vortices.

A few salient features of the vortex system may be noted. The vortex pattern remained fixed in position and the spread of turbulence in the transition region indicates that the direction of rotation is the same for all vortices. There was found only one set of vortices and not the double-layer structure which is indicated by Gregory *et al* (37).

For the present analyses the main conclusion to be drawn from this study is that when present, stationary vortices in the boundary layer are the dominating perturbation. Other perturbations are then of less significance. When no stationary vortices are observed, the transition is delayed until other and less effective disturbances have developed to turbulence.

In the case of viscous instability, the effects of Reynold's number on transition are intimately related to the intensity and frequency spectrum of the disturbances present in the flow (38). This is believed to be the case also for other kinds of instability.

Irregularities on the surface of the body will generate small perturbations in the boundary layer. The spectrum of disturbances will in general be different for the two sides of the body and streamwise-directed vortices may be triggered asymmetrically.

The outcome may be that transition to turbulence will take place far earlier at one side than at the other and in the worst case we have laminar separation at one side and turbulent at the other. In addition, the vortices in the boundary layer will perturb the circulation fed into the wake at separation.

When ordinary viscous instability is initiating turbulence, the flow is more stable. Small perturbations in the Reynold's number are not known to produce abrupt changes in the point of transition. This is a quality intrinsically linked to the appearance of streamwise-directed vortices.

We are looking for instabilities in the flow to explain the large asymmetric forces observed. One of the candidates, which will be investigated further, is the boundary-layer instability with streamwise-directed vortices.

The nature of boundary-layer instability remains an exotic field in fluid mechanics. This is because of the well established, but not fully understood connection between boundary layer instability and transition to turbulence. For any flow it is, in principle, possible to investigate stability properties. The mathematical problem is, however, so complex that certain simplifying assumptions have to be made. First, the disturbance equations are linearized by regarding only small perturbations. Thus, the equations are valid only up to the point where neglected higher order terms become significant. Further, Stuart (37) made a major contribution to the field by showing that for stability analyses "the velocity component in the direction of propagation of the disturbance may be regarded as two-dimensional flow". The problem is thus reduced to the well-known Orr-Sommerfeld equations.

Inspired by Stuart's promising results we shall go a step further by neglecting viscosity. A necessary and sufficient condition for instability is now that the velocity profile has a point of inflection. All other profiles will be stable at the inviscid limit (39).

A fruitful stability analysis under the given assumptions must be made on profiles with a point of inflection. It follows from the inviscid equations that a stationary vortex can develop in the boundary layer only when the point of inflection coincides with a point of zero velocity (37). It is worth noting that the calculations in Chapter 4 gave such profiles just prior to separation.

We choose the last boundary-layer profile calculated before separation at 25 degrees angle of attack (Figure 6.1a) to investigate the structure of the streamwise-directed vortices which may develop. The stability equation at zero viscosity then yields (37)

$$V\left(\frac{\partial^2 w}{\partial \zeta^2} - \sigma^2 w\right) - \frac{\partial^2 V}{\partial \zeta^2} w = 0 \qquad (6.1a)$$

subject to the conditions

$$w = 0 \quad \text{at} \quad \zeta = 0$$

$$w, \frac{\partial w}{\partial \zeta} \to 0 \quad \text{as} \quad \zeta \to \infty \qquad (6.1b)$$

This is an eigenvalue problem and the secondary flow V (Figure 6.1a) is well approximated by

$$V = Ae^{-\alpha\zeta^2} \cdot \sin[f(\zeta)] \qquad (6.1c)$$

where $f(\zeta) \to 2\pi$ as $\zeta \to \infty$ and α is a numerical constant

w is the vertical (ζ-direction) amplitude and σ is the dimensionless wave number of a periodic velocity perturbation.

The eigenvalue problem can be easily converted to a variation problem (37). Multiplication of equation (6.1a) by w and integration yield

$$\sigma^2 = -\int_0^\infty \left(\frac{V''}{V} w^2 + w'^2\right) d\zeta \Big/ \int_0^\infty w^2 d\zeta \qquad (6.2)$$

The eigenvalue σ^2 is now given as the extremal value of equation (6.2) and the belonging w is a solution of the stability problem.

We choose a one-parameter function

$$w = (1+B)e^{-\zeta} - (1+2B)e^{-2\zeta} + B\,e^{-3\zeta} \qquad (6.3)$$

which automatically satisfies the boundary conditions (6.1b). When equation (6.3) is inserted into (6.2) the constant B and the eigenvalue σ^2 are found by numerical optimalization

$$B = -1.325 \qquad (6.4)$$
$$\sigma^2 = 48.7$$

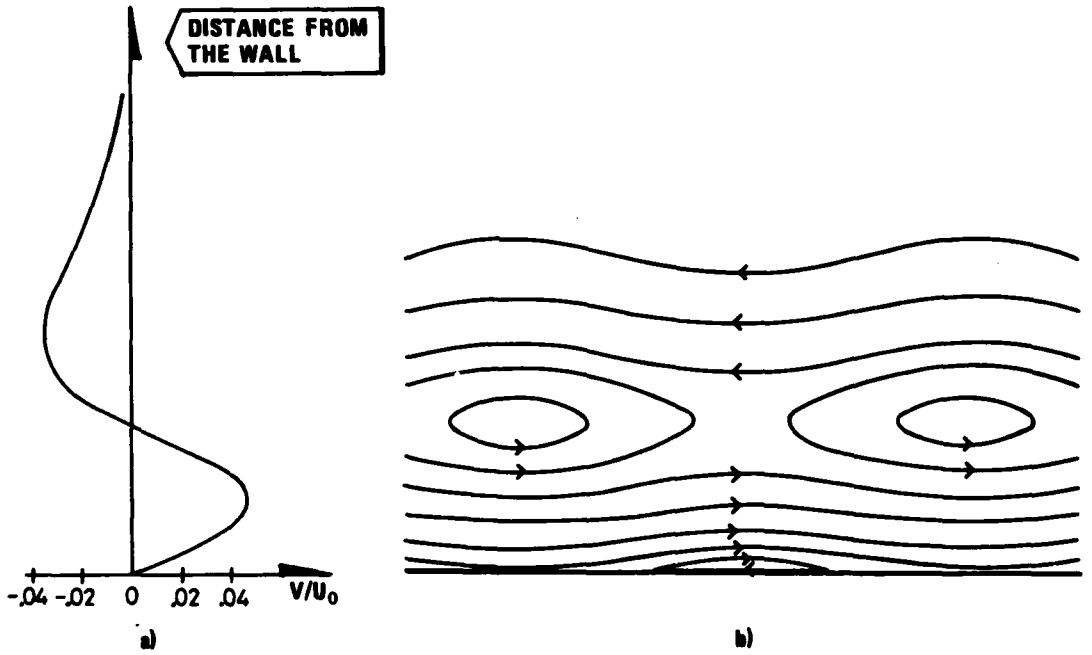

Figure 6.1 a) the secondary velocity profile and b) the calculated streamwise-directed vortices

The streamlines in the disturbed boundary layer will now be calculated. If the free-stream reference velocity is set to 100 m/s and the resulting streamlines in the plane of secondary flow are calculated, we get the flow picture given in Figure 6.1b. This is qualitatively the same vortex system as Stuart (37) calculated for a rotating disk. There are two vortex layers. The vortices close to the surface rotate in one direction and the outer vortices rotate in the opposite direction. In the present case we observe that the inner vortices are extremely close to the surface. The stability calculations have been made without concerning viscosity and thus the velocity perturbation does not satisfy the viscous boundary conditions. When the non-slip condition is imposed

at the surface it seems likely that the inner vortex layer will be wiped out. There then remains a single-layer vortex system where all the vortices rotate in the same direction. This is in agreement with the experimental results reported by Boltz *et al* (36).

Stuart has shown in his inviscid analysis of stability that stationary vortices in the boundary layer may appear only for two-dimensional velocity profiles where the velocity at the point of inflection is zero. Tobak (40) has carried out a similar analysis without neglecting viscous effects. He finds that stationary vortices may appear for profiles differing from Stuart's profile. The viscous corrections are small, however, so the point of inflection has to be close to a point of zero velocity.

The calculated boundary layers in section 4.7 develop the necessary profiles just prior to the primary separation. The streamwise profiles have also inflection points here and the secondary flow cannot be assumed to have such a dominating influence on stability as when it acts together with only viscous destabilizing effects. It is thus unlikely that stationary vortices will develop in the calculated boundary layers.

In Figure 6.1 the spacing of the vortices is of the order of the boundary layer thickness. A properly arranged experiment should therefore reveal the vortices, if present. No such observation is known to the author.

7 ITERATION

The first order calculation of the flow around a circular cone at non-zero angle of attack is concluded. The primary and secondary lines of separation are localized. The boundary layer is calculated for the whole body except between the two lines of separation.

We indicated in Chapter 5 that a process of iteration might be fruitful to improve the results. The present results must then be used as input in a second cycle, and so on.

A second boundary layer calculation where effects of the separated wake are included is then performed. The Kutta-condition imposes a discontinuity on the inviscid two-dimensional cross-flow at separation. This property is included in the first order solution and the second order boundary layer cannot stay attached across the discontinuity. It is thus impossible to have the separation delayed from one step of iteration to the next.

The calculated position of primary separation was compared with experiments in section 4.7. At angles of attack below 24° the separation was predicted prematurely, and further calculations can only worsen this. For higher angles of attack the iteration may improve the first order results.

Convergence in the iteration process cannot be expected and we terminate the calculation with the first order results.

During the calculation of the wake, two-dimensional boundary layer vorticity was fed into the wake from the point of separation. We have argued that the downstream boundary layer does not contribute to the vorticity in the wake. Only the upstream boundary layer has to be considered.

In the first order calculation we assumed that the inviscid surface velocity upstream of separation was not influenced by the separated wake. Figure 7.1 gives the calculated first order cross-flow surface velocity when the effect of the wake is included. The wake has reduced the upstream surface velocity with approximately 30% at separation. This implies that the vorticity flux into the wake is reduced with about 50% compared with the first order solution.

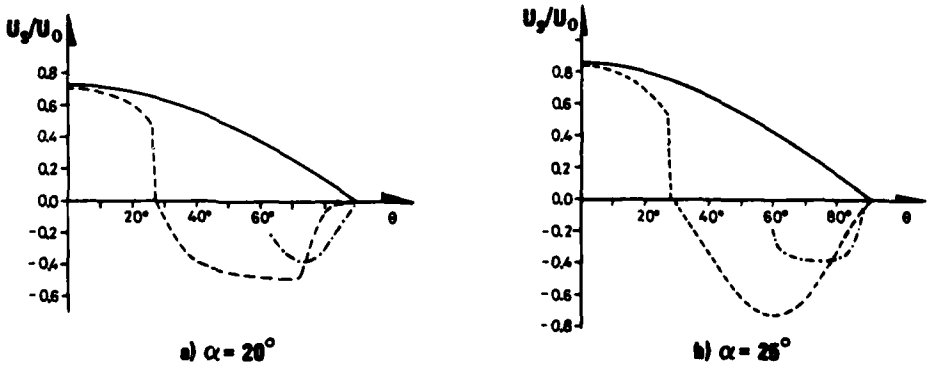

Figure 7.1 The two-dimensional cross flow calculated for the upper half of the cone

——— potential flow

– – – – first order vorticity included

—·—·— second order vorticity included

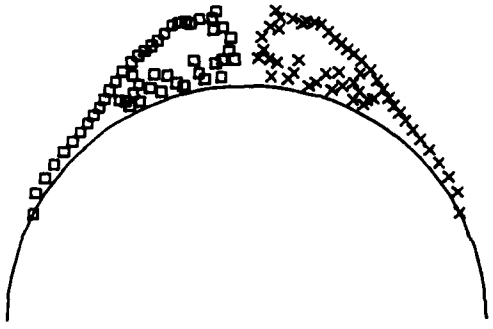

Figure 7.2 The calculated wake with second order vorticity

We consider an angle of incidence of 25°. When the wake is calculated with the full first order vorticity, the vorticies gather in two symmetric domains at the leeside of the body (Figure 5.4c). The typical structure with a feeding sheet and a limited area with distributed vorticity does not result. When the vorticity is halved, however, the observed structure of the wake is obtained (Figure 7.2).

When the two-dimensional surface velocity is calculated with reduced vorticity we get what is reproduced in Figure 7.1. This is quite different from the inviscid surface velocity which the leeside boundary-layer calculations in Chapter 4 were based on.

Leeside boundary-layer calculations have been repeated with the new outer flow. For angle of attack 25° and 20°, separation will take place at 29° and 24°, respectively, from the leeside generator. This is rather close to the observed secondary separation at 25° for both angles of attack considered (25) and a major improvement compared with the first order results (section 4.7).

It is now reasonable to try to pursue the technique of Chapter 5 and introduce discrete vortices at both the primary and secondary line of separation. The idea is to let the vortices develop a wake where circulation from the secondary separation is included.

Secondary vortices are not introduced in the wake before the primary vortices have modified the wake to form a basis for secondary separation. The outcome is that primary and secondary vortices (with opposite circulation) merge to give an unphysical flow picture.

This implies that the technique with discrete vortices cannot be used in modelling a wake which is fed with vorticity from two lines of separation.

In Chapter 8 we shall investigate the stability of the wake when the vorticity is reduced with 50% for all angles of attack considered.

8 STABILITY OF THE WAKE

The primary aim of this thesis is to disclose the cause of the observed asymmetric forces discussed in Chapter 1. Certain perturbations have therefore been introduced in the flow and their downstream development calculated.

In Chapter 6 boundary layer instability was ruled out as the main contributer to the asymmetric forces. Now we shall look into the wake for instabilities.

We neglect the secondary separation and locate the primary lines asymmetrically. In addition to the geometric asymmetry this also implies an asymmetric strength of vorticity. The boundary-layer vortex flux fed into the wake decreases with delayed separation.

Based on experimental indications it is assumed that imperfections at the body's tip initiate the asymmetries. Thus only the first ten point vortices are introduced asymmetrically. We start with the first left-hand vortex displaced 10 degrees in the leeside direction. Over the next 9 vortices this displacement is reduced linearly to zero. The calculation of the downstream development of the wake is performed for angles of incidence ranging from 15 to 60 degrees.

At 15 degrees angle of attack the wake is stable. The nose perturbation is damped and the wake develops with only a slight deviation from symmetry. This is in agreement with the observations at this angle (Figure 8.2).

When the body is pitched to 20 degrees (see Figure 8.1), a small asymmetry in the wake emerges. The wake seems to be so stable that development of substantial asymmetry further downstream on a long body is not expected. This is confirmed by the experimental fact that asymmetric vortex development first appears when the angle of attack exceeds twice the semiapex angle (Figure 8.2).

In agreement with Figure 8.2, the calculated wake (Figure 8.1) is clearly asymmetric for angles above 20 degrees. The effect becomes more pronounced as the body is pitched to higher angles. This is again confirmed by experiments (Figure 8.2). At 50 degrees angle of attack the vorticity from the two sides mixes considerably. There are still, however, two distinct areas on the leeside with surplus of positive and negative circulation, respectively. They are positioned asymmetrically and will impose side forces on the body. When the angle is increased to 60°, the feeding sheets are still intact, but the two domains with concentrated vorticity are wiped out. The wake is brought to disorder and strong asymmetric forces cannot be expected. This is again in agreement with the experimental results by Keener *et al* (Figure 8.2). They find that the time-average side-force diminishes for all but one Reynolds number when the angle of attack exceeds approximately 60°.

The outcome of this stability analysis of the wake is quite remarkable. It not only gives the qualitative development of the wake as the body is pitched through the interesting range of angles. The specific angles where asymmetries first appear and later diminish are quite well predicted.

It further confirms that small perturbations at the tip are capable of triggering the observed lateral forces. The model gives, as previously mentioned, no possibility to incorporate the feedback of the wake on the boundary layers. The state of the wake will influence the location of both primary separation and in particular the secondary separation. Thus the calculations cannot be expected to give an altogether correct picture of the flow.

Figure 8.1 The calculated wake for angles of attack ranging from 20 to 60 degrees when a small perturbation is introduced near the apex

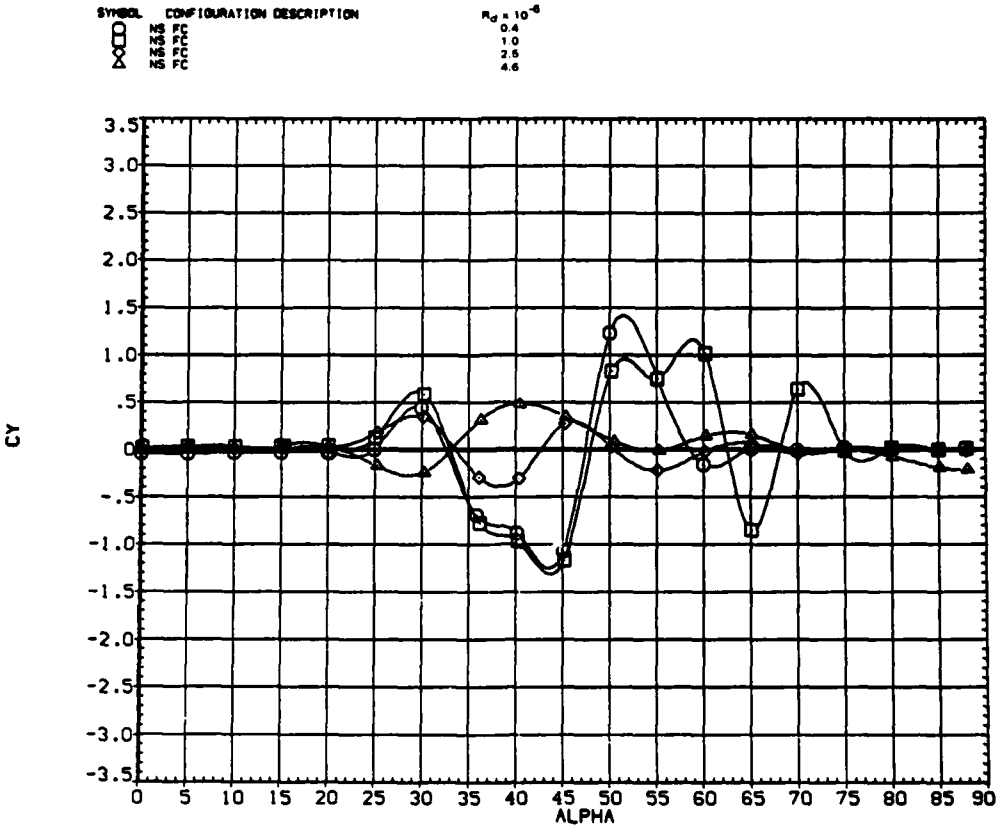

Figure 8.2 Experimental side-force coefficient for various Reynolds numbers as a function of angle of attack (2), M = 0.25
CY = side-force/qS, q = free-stream dynamic pressure, S = base area of the cone

Asymmetric forces are observed for both laminar and turbulent boundary layers (3). This must be expected when the wake instability is the main contributer to asymmetric forces.

Acknowledgements

The work reported here was initiated and for the most part completed during the author's sabbatical year at Division of Aero- and Gas Dynamics, University of Trondheim. In this period financial support was received from the Royal Norwegian Council for Scientific and Industrial Research through a fellowship programme.

The author wishes to express his gratitude to Professor H Nørstrud and Dr T Ytrehus for their assistance throughout the author's dr ing programme.

Special thanks are also due to Superintendent, Dr P Thoresen for support and patience during the completion of this work at Norwegian Defence Research Establishment.

Mrs R Sand, Mrs I Christoffersen, Mrs K Skovli and Mrs R Løken have skilfully typed the manuscript and Mr E Graffer has carefully drawn most of the figures.

APPENDIX A

THE COEFFICIENTS IN THE LINEARIZED MOMENTUM EQUATIONS

$$
\begin{aligned}
a'_n &= w_{l,m,n}/4\cdot\sqrt{s}\Delta\zeta - 0.5/s(\Delta\eta)^2 - (n-1)(u_{l+1,m,n}+u_{l-1,m,n})/16s \\
&\quad -(n-1)\frac{\partial s}{\partial \eta}(v_{l+1,m,n}+v_{l-1,m,n})/8h_2\, s
\end{aligned}
$$

$$
\begin{aligned}
b'_n &= (u_{l+1,m,n}+u_{l-1,m,n})/4h_1\,\Delta\xi + (v_{l,m+1,n}-v_{l,m-1,n})/4h_2\,\Delta\eta \\
&\quad -K_1(u_{l+1,m,n}+u_{l-1,m,n})/4 + 1/s(\Delta\zeta)^2 \\
&\quad -\frac{\partial s}{\partial \eta}(n-1)(v_{l+1,m,n+1}-v_{l+1,m,n-1}+v_{l-1,m,n+1}-v_{l-1,m,n-1})/8h_2\, s
\end{aligned}
$$

$$
\begin{aligned}
c'_n &= -w_{l,m,n}/4\sqrt{s}\Delta\zeta - 0.5/s(\Delta\zeta)^2 + (n-1)(u_{l+1,m,n}+u_{l-1,m,n})/16s \\
&\quad +\frac{\partial s}{\partial \eta}(n-1)(v_{l+1,m,n}+v_{l-1,m,n})/8h_2\, s
\end{aligned}
$$

$$
\begin{aligned}
d'_n &= v_{l-1,m,n}(u_{l+1,m,n}+u_{l-1,m,n})/4h_1\,\Delta\xi - v_{l-1,m,n}(v_{l,m+1,n}-v_{l,m-1,n})/4h_2\,\Delta\eta \\
&\quad -w_{l,m,n}(v_{l-1,m,n+1}-v_{l-1,m,n-1})/4\sqrt{s}\Delta\zeta + K_1 v_{l-1,m,n}(u_{l+1,m,n}+u_{l-1,m,n})/4 \\
&\quad -K_2(u_{l+1,m,n}+u_{l-1,m,n})^2/4 + K_2(u_{l+1,m,N}+u_{l-1,m,N})^2/4 \\
&\quad +(v_{l-1,m,n+1}-2v_{l-1,m,n}+v_{l-1,m,n-1})/2(\Delta\zeta)^2 s \\
&\quad +(n-1)(u_{l+1,m,n}+u_{l-1,m,n})(v_{l-1,m,n+1}-v_{l-1,m,n-1})/16s \\
&\quad +\frac{\partial s}{\partial \eta}(n-1)v_{l-1,m,n}(v_{l-1,m,n+1}-v_{l-1,m,n-1})/8h_2\, s \\
&\quad -\frac{\partial s}{\partial \eta}(n-1)v_{l+1,m,n}(v_{l+1,m,n+1}-v_{l+1,m,n-1})/8h_2\, s
\end{aligned}
$$

$$
\begin{aligned}
a_n &= w_{l,m,n}/4\ \sqrt{s}\Delta\zeta - 0.5/s(\Delta\zeta)^2 - (n-1)(u_{l+1,m,n}+u_{l-1,m,n})/16s \\
&\quad -\frac{\partial s}{\partial \eta}(n-1)(v_{l+1,m,n}+v_{l-1,m,n})/8h_2\, s
\end{aligned}
$$

$$
\begin{aligned}
b_n &= u_{l+1,m,n}/2h_1\,\Delta\xi - K_2(v_{l+1,m,n}+v_{l-1,m,n})/4 + 1/s(\Delta\zeta)^2 \\
&\quad -(n-1)(u_{l+1,m,n+1}-u_{l+1,m,n-1}+u_{l-1,m,n+1}-u_{l-1,m,n-1})/16s
\end{aligned}
$$

$$
\begin{aligned}
c_n &= -w_{l,m,n}/4\sqrt{s}\Delta\zeta - 0.5/s(\Delta\zeta)^2 + (n-1)(u_{l+1,m,n}+u_{l-1,m,n})/16s \\
&\quad +\frac{\partial s}{\partial \eta}(n-1)(v_{l+1,m,n}+v_{l-1,m,n})/8h_2\, s
\end{aligned}
$$

$$
\begin{aligned}
d_n = {} & (u^2_{l+1,m,n} + u^2_{l-1,m,n})/4h_1\Delta\xi - (v_{l+1,m,n} + v_{l-1,m,n})(u_{l,m+1,n} - u_{l,m-1,n})/4h_2\Delta\eta \\
& - w_{l,m,n}\,(u_{l-1,m,n+1} - u_{l-1,m,n-1})/4\sqrt{s}\,\Delta\zeta + K_2\,u_{l-1,m,n}(v_{l+1,m,n} + v_{l-1,m,n})/4 \\
& - K_1(v_{l+1,m,n} + v_{l-1,m,n})^2/4 + (u^2_{l+1,m,N} - u^2_{l-1,m,N})/4h_1\Delta\xi \\
& + (u_{l-1,m,n+1} - 2u_{l-1,m,n} + u_{l-1,m,n})/2s(\Delta\zeta)^2 \\
& + (n-1)u_{l-1,m,n}(u_{l-1,m,n+1} - u_{l-1,m,n-1})/16s \\
& - (n-1)u_{l+1,m,n}(u_{l+1,m,n+1} - u_{l+1,m,n-1})/16s \\
& + \frac{\partial s}{\partial \eta}(n-1)(v_{l+1,m,n} + v_{l-1,m,n})(u_{l-1,m,n+1} - u_{l-1,m,n-1})/8h_2 s
\end{aligned}
$$

APPENDIX B

EXPLICIT REPRESENTATION OF VELOCITY COMPONENTS

The following expression for the complex velocity emerged in section 5.2

$$u-iv = \frac{ik}{2\pi} e^{-i\phi_s} \ln\left(\frac{\sigma-\sigma_A}{\sigma-\sigma_\epsilon}\right) + \frac{ik}{2\pi} e^{i\phi_s}\left\{\left(\frac{r_0}{\sigma}\right)^2 \ln\left(\frac{\sigma\bar{\sigma}_A - r_0^2}{\sigma\bar{\sigma}_\epsilon - r_0^2}\right) + \frac{\bar{\sigma}_A}{\sigma} - \frac{\bar{\sigma}_\epsilon}{\sigma}\right\} \tag{B.1}$$

The endpoints of the vortex sheet are (Figure B.1)

$$\sigma_A = r_0 e^{i\theta_s} + Ae^{i\phi_s} \tag{B.2}$$

$$\sigma_\epsilon = (r_0 + \epsilon)e^{i\theta_s} \tag{B.3}$$

We are interested only in the velocities on the surface of the body. Thus

$$\sigma = r_0 e^{i\theta} \tag{B.4}$$

To make the calculations more surveyable, we split equation (B.1) and start with

$$\ln\left(\frac{\sigma-\sigma_A}{\sigma-\sigma_\epsilon}\right) = \ln\left[e^{i\theta} - e^{i\theta_s} - \frac{A}{r_0} e^{i\phi_s}\right] - \ln\left[e^{i\theta} - \left(1+\frac{\epsilon}{r_0}\right)e^{i\theta_s}\right] =$$

$$\ln\left[\cos\theta - \cos\theta_s - \frac{A}{r_0}\cos\phi_s + i(\sin\theta - \sin\theta_s - \frac{A}{r_0}\sin\phi_s)\right] -$$

$$\ln\left[\cos\theta - \left(1+\frac{\epsilon}{r_0}\right)\cos\theta_s + i\left\{\sin\theta - \left(1+\frac{\epsilon}{r_0}\right)\sin\theta_s\right\}\right] \tag{B.5}$$

With the following substitutions

$$A_1 = \cos\theta - \cos\theta_s - \frac{A}{r_0}\cos\phi_s$$

$$A_2 = \sin\theta - \sin\theta_s - \frac{A}{r_0}\sin\phi_s$$

$$A_3 = \cos\theta - \left(1+\frac{\epsilon}{r_0}\right)\cos\theta_s$$

$$A_4 = \sin\theta - \left(1+\frac{\epsilon}{r_0}\right)\sin\theta_s \tag{B.6}$$

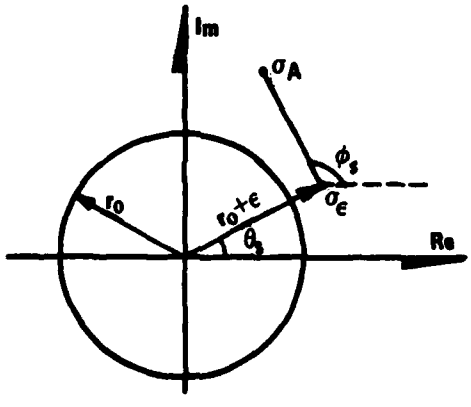

Figure B.1 The geometry of the calculation

we get as first term

$$\frac{ik}{2\pi} e^{-i\phi_s} \ln\left(\frac{\sigma-\sigma_A}{\sigma-\sigma_\epsilon}\right) = \frac{k}{2\pi}(i\cos\phi_s + \sin\phi_s) \cdot \left\{ \frac{1}{2}\ln\left(\frac{A_1^2+A_2^2}{A_3^2+A_4^2}\right) + i\left[\operatorname{arctg}\left(\frac{A_2}{A_1}\right) - \operatorname{arctg}\left(\frac{A_4}{A_3}\right)\right]\right\} = u_1 - iv_1 \qquad (B.7)$$

which yields

$$\begin{aligned} u_1 &= \frac{k}{4\pi}\ln\left[\frac{A_1^2+A_2^2}{A_3^2+A_4^2}\right]\sin\phi_s - \frac{k}{2\pi}\left[\operatorname{arctg}\left(\frac{A_2}{A_1}\right) - \operatorname{arctg}\left(\frac{A_4}{A_3}\right)\right]\cos\phi_s \\ v_1 &= -\frac{k}{4\pi}\ln\left[\frac{A_1^2+A_2^2}{A_3^2+A_4^2}\right]\cos\phi_s - \frac{k}{2\pi}\left[\operatorname{arctg}\left(\frac{A_2}{A_1}\right) - \operatorname{arctg}\left(\frac{A_4}{A_3}\right)\right]\sin\phi_s \end{aligned} \qquad (B.8)$$

The second term is

$$\frac{ik}{2\pi}\left(\frac{\bar{\sigma}_A - \bar{\sigma}_\epsilon}{\sigma}\right) e^{i\phi_s} = \frac{ik}{2\pi}\left[\frac{A}{r_0} e^{-i\theta} - \frac{\epsilon}{r_0} e^{i(\phi_s - \theta_s - \theta)}\right] = u_2 - iv_2 \qquad (B.9)$$

which implies

$$\begin{aligned} u_2 &= \frac{k}{2\pi r_0}\left[A\sin\theta + \epsilon\sin(\phi_s - \theta_s - \theta)\right] \\ v_2 &= -\frac{k}{2\pi r_0}\left[A\cos\theta - \epsilon\cos(\phi_s - \theta_s - \theta)\right] \end{aligned} \qquad (B.10)$$

For calculation of the third term we start with

$$\ln\left[\frac{\sigma\bar{\sigma}_A - r_0^2}{\sigma\bar{\sigma}_\epsilon - r_0^2}\right] = \ln\left[\frac{r_0^2 e^{i(\theta-\theta_s)} + r_0 A e^{i(\theta-\phi_s)} - r_0^2}{r_0(r_0+\epsilon)e^{i(\theta-\theta_s)} - r_0^2}\right] =$$

$$\ln\left\{\cos(\theta-\theta_s) + \frac{A}{r_0}\cos(\theta-\phi_s) - 1 + i\left[\sin(\theta-\theta_s) + \frac{A}{r_0}\sin(\theta-\phi_s)\right]\right\} -$$

$$\ln\left\{\left(1+\frac{\epsilon}{r_0}\right)\cos(\theta-\theta_s) - 1 + i\left(1+\frac{\epsilon}{r_0}\right)\sin(\theta-\theta_s)\right\} \qquad (B.11)$$

With the following substitutions

$$\begin{aligned} B_1 &= \cos(\theta-\theta_s) + \frac{A}{r_0}\cos(\theta-\phi_s) - 1 \\ B_2 &= \sin(\theta-\theta_s) + \frac{A}{r_0}\sin(\theta-\phi_s) \\ B_3 &= \left(1+\frac{\epsilon}{r_0}\right)\cos(\theta-\theta_s) - 1 \\ B_4 &= \left(1+\frac{\epsilon}{r_0}\right)\sin(\theta-\theta_s) \end{aligned} \qquad (B.12)$$

we get

$$\frac{ik}{2\pi}\left(\frac{r_0}{\sigma}\right)^2 \ln\left(\frac{\sigma\bar{\sigma}_A - r_0^2}{\sigma\bar{\sigma}_\epsilon - r_0^2}\right) =$$

$$\frac{k}{2\pi}[i\cos(\phi_s - 2\theta) - \sin(\phi_s - 2\theta)]\left\{\frac{1}{2}\ln\left(\frac{B_1^2+B_2^2}{B_3^2+B_4^2}\right) + i\left[\operatorname{arctg}\left(\frac{B_1}{B_2}\right) - \operatorname{arctg}\left(\frac{B_3}{B_4}\right)\right]\right\} = u_3 - iv_3 \tag{B.13}$$

which yields

$$\begin{aligned} u_3 &= -\frac{k}{4\pi}\ln\left[\frac{B_1^2+B_2^2}{B_3^2+B_4^2}\right]\sin(\phi_s - 2\theta) - \frac{k}{2\pi}\left[\operatorname{arctg}\left(\frac{B_1}{B_2}\right) - \operatorname{arctg}\left(\frac{B_3}{B_4}\right)\right]\cos(\phi_s - 2\theta) \\ v_3 &= \frac{k}{2\pi}\left[\operatorname{arctg}\left(\frac{B_1}{B_2}\right) - \operatorname{arctg}\left(\frac{B_3}{B_4}\right)\right]\sin(\phi_s - 2\theta) - \frac{k}{4\pi}\ln\left[\frac{B_1^2+B_2^2}{B_3^2+B_4^2}\right]\cos(\phi_s - 2\theta) \end{aligned} \tag{B.14}$$

The velocity components in equation (B.7) may now be written

$$u = u_1 + u_2 + u_3$$

$$v = v_1 + v_2 + v_3$$

where the right sides are explicitly given by equations (B.8), (B.10) and (B.14).

References

(1) Allan H J, Perkins E W (1951): A study of effects of viscosity on flow over slender inclined bodies of revolution, NACA Report 1048.

(2) Keener E R, Chapman G T, Cohen L, Taleghani J (1977): Side forces on a tangent ogive forebody with a fineness ratio of 3.5 at high angles of attack and Mach numbers from 0.1 to 0.7, NASA TM X–3437.

(3) Jorgensen L H, Nelson E R (1974): Experimental aerodynamic characteristics for a cylindrical body of revolution with various noses at angles of attack from 0° to 58° and Mach numbers from 0.6 to 2.0, NASA TM X–3128.

(4) Coe P L, Chambers J R, Letko W (1972): Asymmetric lateral-directional characteristics of pointed bodies of revolution at high angles of attack, NASA TN D–7095.

(5) Keener E R, Chapman G T, Cohen L, Taleghani J (1977): Side forces on forebodies at high angles of attack and Mach numbers from 0.1 to 0.7. Two tangent ogives, paraboloid and cone, NASA TM X–3438.

(6) Deffenbaugh F D, Koerner W G (1977): Asymmetric vortex wake development on missiles at high angles of attack, *J Spacecraft and Rockets* 14, 3, 155–62.

(7) Pick G S (1972): Side forces on ogive-cylinder bodies at high angles of attack in transonic flow, *J Spacecraft and Rockets* 9, 6, 389–90.

(8) Wardlaw A B Jr, Morrison A M (1975): Induced side forces on bodies of revolution at high angle of attack, NSWC/WOL/TR 75–176, Naval Surface Weapons Center, White Oak, Md.

(9) Angelucci S B (1971): A multivortex method for axisymmetric bodies at angle of attack, *J Aircraft* 8, 12, 959–66.

(10) Marshall F J, Deffenbaugh F D (1974): Separated flow over bodies of revolution using an unsteady discrete-vorticity cross wake. Part I – Theory and application, NASA CR–2414.

(11) Smith J H B (1975): A review of separation in steady, three-dimensional flow, AGARD–CP–168, paper 31.

(12) Hess J L, Smith A M O (1967): Calculation of potential flow about arbitrary bodies, *Prog Aeronant Sci* 8, Pergamon Press, 1–138.

(13) Kanwal R P (1971): Linear integral equations, ch 6, Academic Press.

(14) Dahlquist G, Björk A (1974): Numerical methods, Prentice-Hall, New Jersey.

(15) White F M (1974): Viscous fluid flow, McGraw-Hill.

(16) Hall M G (1967): A numerical method for calculating steady three-dimensional laminar boundary layers, RAE TR 67145.

(17) Geissler W (1975): Calculation of three-dimensional laminar boundary layer around bodies of revolution at incidence and with separation, AGARD–CP–168, paper 33.

(18) Cebeci T, Kaups K, Mosinskis G J, Rehn J A (1973): Some problems of the calculation of three-dimensional boundary-layer flows on general configurations, NASA CR–2285.

(19) Peake D J, Owen F K, Higuchi H (1978): Symmetrical and asymmetrical separations about a yawed cone, AGARD–CP–247.

(20) Roache P J (1976): Computational fluid dynamics, Hermosa publishers, New Mexico.

(21) Howarth L (1951): The boundary layer in three-dimensional flow. Part 2 – The flow near a stagnation point, *Phil Mag* 42, 1433–40.

(22) Landan L D, Lifshitz E M (1966): Fluid mechanics, Pergamon Press.

(23) Werlé H (1975): Écoulement décollés, Étude phénoménologique a partir de visualisations hydrodynamiques, AGARD–CP–168, paper 39.

(24) Mangler W (1948): *Z Angew Math Mech* 28, 97–103.

(25) Rainbird W J, Crabbe R S, Jurewicz L S (1963): A water tunnel investigation of the flow separation about circular cones at incidence, Aero Report LR–385, Nat Res Council, Ottawa, Canada.

(26) Maskell E C (1955): Flow separation in three dimensions, RAE Report Aero 2565, ARC 18063.

(27) Schliching H (1968): Boundary layer theory, McGraw-Hill, New York.

(28) Ashley H, Landahl M (1965): Aerodynamics of wings and bodies, Addison-Wesley.

(29) Sachs A H, Lundberg R E, Hanson C W (1967): A theoretical investigation of the aerodynamics of slender wing and body combinations exhibiting leading-edge separation, NASA CR–719.

(30) Smith J H B (1977): Behaviour of a vortex sheet separating from a smooth surface, RAE TR 77058.

(31) Batchelor G K (1967): An introduction to fluid dynamics, Cambridge University Press.

(32) Nielsen J N (1960): Missile aerodynamics, McGraw-Hill.

(33) Edwards R H (1954): Leading edge separation from delta wings, *J Aeronaut Sci* 21, 134.

(34) Brown C E, Michael W H (1955): On slender delta wings with leading-edge separation, NACA TN–3430.

(35) Grimson J (1958): An investigation into flow separation from cones at low speed. Some of the results are found in (25). Unpublished.

(36) Boltz F W, Kenyon G C, Allan C Q (1960): Effects of sweep angle on the boundary-layer stability characteristics of an untapered wing at low speeds, NASA TN D–338.

(37) Gregory N, Stuart J T, Walker W S (1955): On the stability of three-dimensional boundary layers with application to the flow due to a rotating disk, *Phil Trans ser A* 248, 155–99.

(38) Schubauer G B, Skramstad H K (1947): NACA Rep 909.

(39) Rayleigh, Lord (1964): Scientific Papers, Vol 1, Dover, New York, 474–87.

(40) Tobak M (1973): On local inflexional instability in boundary-layer flows, *J Appl Math Phys* 24, 330–54.


FILME
7-8